Detailed nucleation process and mechanism of the July 2019 Mw 6.4 Ridgecrest, California earthquake

Min Liu[1], Miao Zhang[2], and Hongyi Li[1]

[1]China University of Geosciences (Beijing)
[2]Dalhousie University

November 30, 2022

Abstract

We utilized the Match&Locate method to characterize the detailed spatial and temporal evolution of earthquakes before the July 2019 Mw 6.4 Ridgecrest, California earthquake. The Mw 6.4 mainshock was preceded by 40 foreshocks within ~2 h (on July 4, 2017 from 15:35:29 to 17:32:52, UTC). The largest foreshock (M 4.0) separates the foreshock activity into two stages with different nucleation mechanisms. A swarm of repeating earthquakes occurred before the M 4.0 event, implying the earthquake sequence initiated from an aseismic slip process. The majority of aftershocks of the M 4.0 event as well as the Mw 6.4 mainshock, occurred within regions of increasing Coulomb stress, indicating that they were triggered by stress transfer. Our observations demonstrate that neither the preslip model nor the cascade model can explain the entire nucleation process of the Mw 6.4 mainshock. Instead, both mechanisms govern the nucleation process, but at different stages.

Posted on 30 Nov 2022 — CC-BY-NC-ND 4 — https://doi.org/10.1002/essoar.10503605/v1 — This a preprint and has not been peer reviewed. Data may be preliminary.

Detailed nucleation process and mechanism of the July 2019 Mw 6.4 Ridgecrest, California earthquake

Min Liu[1,2], Miao Zhang[2*] and Hongyi Li[1*,3]

[1]School of Geophysics and Information Technology, China University of Geosciences (Beijing), Beijing, China

[2]Department of Earth and Environmental Sciences, Dalhousie University, Halifax, Nova Scotia, Canada

[3]Shanghai Sheshan National Geophysical Observatory, Shanghai, China

Corresponding author: Miao Zhang (miao.zhang@dal.ca) and Hongyi Li (lih@cugb.edu.cn)

Key points:

- We detected and located 40 foreshocks of the July 2019 Mw 6.4 Ridgecrest earthquake using the Match&Locate method.
- The detailed spatiotemporal evolution of the foreshocks outlines a complex fault system accommodating the nucleation of the Mw 6.4 mainshock.
- The nucleation of the Mw 6.4 earthquake could be jointly explained by the preslip and cascade models.

Abstract

We utilized the Match&Locate method to characterize the detailed spatial and temporal evolution of earthquakes before the July 2019 Mw 6.4 Ridgecrest, California earthquake. The Mw 6.4 mainshock was preceded by 40 foreshocks within ~2 h (on July 4, 2017 from 15:35:29 to 17:32:52, UTC). The largest foreshock (M_L 4.0) separates the foreshock activity into two stages with different nucleation mechanisms. A swarm of repeating earthquakes occurred before the M_L 4.0 event, implying the earthquake sequence initiated from an aseismic slip process. The majority of aftershocks of the M_L 4.0 event as well as the Mw 6.4 mainshock, occurred within regions of increasing Coulomb stress, indicating that they were triggered by stress transfer. Our observations demonstrate that neither the preslip model nor the cascade model can explain the entire nucleation process of the Mw 6.4 mainshock. Instead, both mechanisms govern the nucleation process, but at different stages.

Plain Language Summary

The 2019 Mw 6.4 Ridgecrest, California earthquake was preceded by a significant foreshock sequence in the ~2 h leading up to the main shock, presenting a question: what is the relationship between the Mw 6.4 mainshock and its foreshocks? In this study, we comprehensively analyzed seismograms obtained from nine nearby stations before the Mw 6.4 earthquake using state-of-the-art methods. Our unprecedented high-precision earthquake catalog demonstrates the detailed spatiotemporal evolution of the foreshocks. We investigated the nucleation mechanism for the foreshocks based on the relationship between their accurate hypocenters and the nearby stress changes. Our study suggests that aseismic slip and stress transfer jointly explain the nucleation mechanism of the Mw 6.4 mainshock.

1 Introduction

The July 2019 Ridgecrest earthquake sequence broke a nearly 20-year absence of strong earthquakes in southern California. This sequence included two closely-spaced (about 10 km apart; Figure 1) mainshocks: an Mw 6.4 event on 4 July, 2019 (at 17:33:49 UTC) and an Mw 7.1 event on 6 July 2019 (at 03:19:53 UTC). The two mainshocks activated a complex fault network, consisting of the main NW-trending fault with about 65 km surface rupture, the NE-trending cross fault with 15 km surface rupture, as well as multiple near-orthogonal buried faults which cut through the main fault (Figure 1) (Liu et al., 2020; Ross et al., 2019; Shelly, 2020; Yang et al., 2020). The Southern California Seismic Network (SCSN) reported 9 foreshocks in ~2 h preceding the Mw 6.4 mainshock. Although the foreshock catalog has been further improved using state-of-the-art techniques, such as the template matching technique (Ross et al., 2019; Shelly, 2020) and a machine-learning-based phase picker (Liu et al., 2020), the relationship between the Mw 6.4 mainshock and its foreshocks (i.e., nucleation mechanism) is not well understood.

Two opposing models have been proposed to explain earthquake nucleation: the preslip model and the cascade model (Beroza & Ellsworth, 1996; Dodge et al., 1996; Ellsworth & Beroza, 1995; Mignan, 2014). In the preslip model, foreshocks are attributed to aseismic slip surrounding the eventual mainshock hypocenter and may appear as repeating earthquakes. This model provides the possibility for earthquake prediction (Bouchon et al., 2011; Chen and Shearer, 2013; Dodge et al., 1996; Kato et al., 2012; McGuire et al., 2005; Savage et al., 2017; Tape et al.,. 2018). In the cascade model, later earthquakes usually occur in regions of increasing stress, which are triggered by adjacent preceding events (Ellsworth and Bulut, 2018; Felzer et al., 2004; Helmstetter and Sornetter, 2003; Yoon et al., 2019). In other words, under this model, earthquakes, even the large ones, are random outcomes of triggering, implying that earthquake prediction is impossible (Ellsworth & Beroza, 1995). Recently, a combination of both mechanisms has been proposed to understand the complex nucleation process of some large earthquakes (Savage et al., 2017; Yao et al., 2020).

A comprehensive and high-precision earthquake catalog plays a key role in understanding the underlying earthquake nucleation mechanism. Using a matched filter is a promising technique for small earthquake detection, and involves the application of cross-correlation (CC) between the template events and continuous waveforms (Gibbons & Ringdal, 2006). Because this process assumes that the newly detected earthquakes are co-located with template events, the matched filter is only capable of detecting closely adjacent earthquakes and cannot provide accurate location information. Thus, earthquakes must be relocated separately using sequential algorithms such as cross-correlation and double-difference relocation (e.g., Ellsworth & Bulut, 2018; Yao et al., 2020; Yoon et al., 2019). Each of the above steps may affect the final earthquake catalog, from magnitude completeness to location accuracy. For instance, cross-correlation differential travel times are only maintained for waveform pairs with very high similarity (e.g., CC > 0.7), which potentially decreases the number of available template phases/stations and lowers the location resolution. To solve this issue, Zhang and Wen (2015a) developed the Match&Locate method (M&L) to simultaneously detect and locate earthquakes, using all available components and stations, by maximizing the stacked waveform coherence based on the delay-and-sum concept. One remarkable application of this method was the detection and location of a controversial low-yield nuclear test conducted by North Korea in 2010, providing seismological evidence of the nuclear explosion along with radionuclide findings (Zhang & Wen, 2015b).

To understand the nucleation mechanism of the July 2019 Mw 6.4 Ridgecrest mainshock, we comprehensively investigated the relationship between the Mw 6.4 mainshock and its foreshocks. By applying the M&L method, we built a comprehensive and high-precision earthquake catalog of the foreshocks and determined the rupture directivity of the largest M_L 4.0 foreshock, by estimating its initial point and centroid point, as well as the initial point of the Mw 6.4 mainshock. Waveform similarity analysis and Coulomb stress change calculations were also adopted, to investigate the nucleation process.

2 Detailed spatiotemporal evolution of foreshocks

We used the M&L method to detect and locate earthquakes before the Mw 6.4 mainshock (from 15:35:26 to 17:32:52, UTC on July 4, 2019). Continuous seismic data were collected from nine permanent stations within 60 km of the Mw 6.4 mainshock (Figure 1). We selected the M_L 1.5 foreshock as the template event (EQ 6; see Table S1 in the supporting information), as it had a moderate magnitude and relatively high similarity to other SCSN cataloged foreshocks. The location of the template event was extracted from the cross-correlation hypoDD catalog (Shelly, 2020). We adopted the same 1-D velocity model suggested by Shelly (2020).

To efficiently conduct the M&L method, we built the foreshock catalog in two steps. The first step involved detecting and roughly locating earthquakes from continuous waveforms, while the second step involved refining their locations. In the first step, we searched for potential earthquakes within a 3D region centered at the template location: $0.006° \times 0.006° \times 600$ m in longitude, latitude, and depth, with a searching interval of 0.0006° laterally (i.e., approximately 60 m) and 60 m vertically. Both P and S phases were utilized in the M&L method. We used the TauP software to calculate the theoretical P- and S-wave arrival times for the template event, as well as their horizontal and vertical slowness (Crotwell et al., 1999; Zhang and Wen, 2015a). The template windows were 0.2 s before and 1.8 s after their theoretical arrival times. Such window settings enable us to separate P and S phases into corresponding time windows. We kept the default 100 Hz sampling interval for this step. We filtered the template and continuous waveforms from 2 to 12 Hz to improve the signal-to-noise ratio. With an empirical CC threshold of 0.35, we detected and located 39 foreshocks with magnitudes ranging from -0.39 to 4.0 (Figure 1; Table S1). Here, both location and magnitude were determined relative to the template event (see detailed method introduction in Zhang and Wen, 2015a). The second step focuses on refining the location of the events detected in the first step. Waveforms of the 39 detected events were cut from 5 s before and 25 s after their origin time. Earthquake locations were further refined within a smaller 3D region, with a finer search grid size centered at the optimal locations determined in the first step: $0.001° \times 0.001° \times 100$ m in longitude, latitude, and depth with a searching interval of 0.00001° laterally (i.e., approximately 1 m) and 1 m vertically. To match this high spatial resolution, we interpolated the template and continuous waveforms from 100 to 5000 Hz. All 39 earthquakes were relocated with high precision, which can be verified by waveform comparison between them and the template event along with their CC spatial convergence (see Text S1). Based on a bootstrapping analysis, the horizontal and vertical location uncertainties are determined to be 3–8 m and 3–10 m, respectively (see Text S1). All 35 events reported in the CC hypoDD catalog were recovered with the M&L method (Shelly, 2020). Even though they are independently located with different algorithms and slightly different stations, the common events are consistent in space with an average hypocentral separation of 34.2 m, except for the 20190704T17:16:50 event, which was mislocated in the hypoDD catalog (Figures S1-2).

This unprecedented high-precision catalog enables us to reveal detailed spatiotemporal migration of foreshocks and delineate the fine-scale structure of the fault zone (Figures 2a-e and Movie S1). On July 4, 2019 at 15:35:26 (UTC), a burst of small earthquakes began activating near the hypocenter of the Mw 6.4 mainshock (Figure 2a). After 45 min of silence, the largest M_L 4.0 foreshock nucleated nearby (Figure 2b). In the following 9 min, its early aftershocks occurred along a SW-dipping fault around its hypocenter (Figure 2b). Later on, a NW-trending shallow fault strand and a nearly north-trending deep low-dip fault strand were sequentially activated, and were gradually connected by later earthquakes before the occurrence of the Mw 6.4 mainshock, forming a throughgoing fault structure (Figure 2d).

3 Rupture directivity analysis of M_L 4.0 foreshock

We conducted rupture directivity analysis for the M_L 4.0 earthquake. Based on the empirical Green's function method, similar to the relative directivity inversion method proposed by Xu and Wen (2019), we directly estimated the initial rupture point and centroid point of the M_L 4.0 earthquake using the M&L method. However, instead of minimizing the CC travel-time residual, the M&L method determines the two points by grid-searching the optimal location to maximize the averaged CC coefficient between the target event and the master event. Here, we kept the M_L 1.5 event as our master event because of its high signal-to-noise ratio, high similarity, and suitable magnitude. We utilized the initial P phases and full P and S phases to investigate the initial rupture point and centroid point, respectively. We used the same data processing techniques that were used to build the foreshock catalog in step 2. The centroid point was extracted directly from our high-precision foreshock catalog. In the initial point estimation, we manually picked the first P-wave arrivals on vertical components and set a template window of 0.03 s before and 0.03 s after the P-wave arrivals. The results indicate that the M_L 4.0 foreshock ruptured unilaterally along the NW fault with a rupture length of 630 m (i.e., twice the distance between the initial rupture point and centroid point), which is consistent with one of the reported nodal fault planes (SCSN; Figures 3a-b). Similarly, we determined the initial rupture point for the Mw 6.4 mainshock, which is located about 75 m SE of the master event (Figures 3c-d). Here, station SLA was not adopted due to the poor similarity between the Mw 6.4 event and the master event (Figure S3). The centroid point of the Mw 6.4 mainshock cannot be estimated in this way because of the complexity of its rupture in space and time.

4 Nucleation of the Mw 6.4 mainshock and its foreshocks

We conducted further studies to determine whether the preslip model or cascade model could explain the nucleation mechanism of the Mw 6.4 mainshock. Repeating earthquakes (REs) occur on the same or overlapping fault areas (patch) and support the preslip model, but cannot be explained by the cascade model (Ellsworth & Beroza, 1995). Thus, the identification of REs plays a critical role in distinguishing the two nucleation mechanisms.

REs are identified using two sequential criteria: 1) events must have high waveform similarity and 2) events must rupture on overlapping faults/patches (Uchida, 2019; Uchida and Burgmann, 2019). To perform similarity analysis, we calculated the pairwise cross-correlation for the 40 foreshocks based on the vertical component of the closest station, B918 (Figure 1). Waveform windows were cut from 1 s before and 6 s after the first P-wave arrivals, including the whole S-wave phases and most coda waves. A maximum 0.2 s lag was adopted during the cross-correlation. Based on a CC threshold of 0.9 (Uchida and Burgmann, 2019), we grouped corresponding events into clusters using the equivalency class algorithm (Press et al., 1986). Two candidate earthquake clusters were identified: six events before the M_L 4.0 earthquake (EQ 2–7; Table S1) and twelve shallow events following the M_L4.0 earthquake (Figure 2f). Here, we have assigned the first earthquake (EQ 1) of the whole sequence to the first cluster, even though it possesses a relatively low CC coefficient (0.65–0.73) with others in the cluster. This is because the event is located very close to the center of the cluster (Figure 2a and Movie S1). The low CC value is caused by waveform overlapping (the event was closely followed by a larger event with an origin time separation of 3 s) (Figure 2f). Therefore, we have seven earthquakes in the first cluster. The seven events occurred within a radius of 25 m, which is less than the theoretical 31-m rupture radius of the largest event (M_L1.5) among the cluster (Figure 2a; see Text S2). In other words, their rupture patches were at least partially overlapping. Thus, we regard them as an RE cluster. The second cluster of events shows an NW-trending extent of ~200 m (Figure 2d), which is far beyond the theoretical 50-m rupture radius of the largest event (M_L 2.15) among the cluster (see Text S2). Thus, we rule out the possibility that they belong to an RE cluster, based on the second criterion. Based on the above analysis, we suggest that the foreshock sequence was activated from a cluster of REs and earthquakes before the M_L 4.0 event initiated from an aseismic-slip process.

To determine whether the cascade model can explain the events following the M_L4.0 earthquake and the Mw 6.4 mainshock, we verified the potential triggering mechanism by investigating the relationship between the hypocenters of those events and the nearby stress changes. Two different approaches were applied to estimate the stress changes. In the first approach, we inverted the Coulomb stress change according to the focal mechanism solution of the M_L4.0 event (Lin & Stein, 2004). The initial rupture point of the M_L4.0 foreshock estimated by the M&L method, one of the fault planes that matched rupture directivity (i.e., strike = 318°, rake = 167°, and dip = 81°; SCSN), and a recommended friction coefficient of 0.4 were adopted in the Coulomb stress change inversion (Lin & Stein, 2004; Toda et al., 2005). The majority of the aftershocks of the M_L 4.0 event, as well as the Mw 6.4 mainshock, nucleated in the regions with increasing Coulomb stress (Figures 4a-c), which suggests they were triggered by stress transfer. In the second approach, we empirically inferred the stress change imparted by the M_L4.0 event in space based on a simple circular crack (Kanamori & Anderson, 1975). From our previous directivity analysis, we know that the largest possible rupture radius of the M_L4.0 event is 315 m (blue circle in Figure 4d). Earthquakes following the M_L4.0 earthquake as well as the Mw 6.4 mainshock, dominantly occurred outside of the rupture zone of the M_L4.0 event (Figure 4d), which usually indicates increased stress (Ellsworth & Bulut, 2018; Yoon et al., 2019). The two independent analyses suggest that the majority of aftershocks of the M_L 4.0 earthquake and Mw

6.4 mainshock were triggered by stress transfer, which is in line with the cascade model. We also noticed that a few earthquakes likely re-ruptured the source zone of the M_L4.0 event (Figure 4d), which may be explained by aseismic slip or rupture heterogeneity (Ellsworth & Bulut, 2018).

5 Discussion

Direct and robust evidence indicates that the preslip model and cascade model jointly governed the nucleation process of the Mw 6.4 mainshock. A cluster of REs preceding the largest M_L 4.0 foreshock occurred within a radius of 25 m (Figure 2a), consistent with the small nucleation zone of an M_L 4.0 earthquake (Dodge et al., 1996; Ellsworth & Beroza, 1995). The magnitude of the members in the RE cluster shows an overall increasing trend prior to the occurrence of the M_L 4.0 foreshock (Figure 2e), in accordance with the reported accelerating slip process (Kato et al., 2012, 2016; Tape et al., 2018). The majority of aftershocks of the M_L 4.0 earthquake, as well as the Mw 6.4 mainshock, were triggered by the stress change imparted by the M_L 4.0 event (Figure 4), consistent with the cascade triggering process described in previous studies (Ellsworth & Bulut, 2018; Yao et al., 2020; Yoon et al., 2019). A similarly complex nucleation process was also observed in the foreshock sequence of the 2010 Mw 7.2 EI Mayor-Cucapah earthquake (Yao et al., 2020). Here, as a complete explanation for the nucleation process of the Mw 6.4 earthquake, we suggest that the aseismic slip process initiated the nucleation, and cascade triggering dominated the following events. The coalescence of aseismic slip and transferred stress triggering in earthquake nucleation has been implied from laboratory experiments and numerical models (Dublanchet, 2018; McLaskey, 2019; McLaskey & Lockner, 2014; Noda et al., 2013). Our study bridges the gap between laboratory experiments and field observations.

Immature fault systems that are transitioning into new major tectonic boundaries are usually characterized by a geometrically complex fault distribution and slow earthquake rupture (Crider & Peacock, 2004). Source inversion suggests that the Mw 6.4 and Mw 7.1 events ruptured with a slow velocity of about 1-2 km/s (Chen et al., 2020; Goldberg et al., 2020; Ross et al., 2019; Yang et al., 2020). Goldberg et al. (2020) concluded that the 2019 Ridgecrest sequence occurred on an immature fault. In this study, our foreshock catalog reveals a complex seismogenic structure, consisting of at least three fault strands with variable orientations (Figure 2), which independently supports the notion that the 2019 Ridgecrest sequence nucleated on an immature fault system. These individual fault strands are in fact small and may not be optimally oriented for large-scale earthquake failure (Crider & Peacock, 2004). However, a throughgoing fault structure was connected by the earthquakes following the Mw 4.0 event (Figure 2d), and accommodated the Mw 6.4 mainshock (Goldberg et al., 2020; Manighetti et al., 2007; Perrin et al., 2016; Thomas et al., 2013; Wesnousky, 1988).

6 Conclusions

We applied the M&L method to comprehensively investigate the detailed spatiotemporal evolution of foreshocks of the Mw 6.4 earthquake and to directly estimate rupture directivity and rupture length of its largest foreshock (M_L 4.0). We identified 40 foreshocks that occurred ~2 h before the mainshock, with magnitudes ranging from −0.39 to 4.0. The largest M_L 4.0 foreshock separated the sequence into two stages with different nucleation mechanisms. The nucleation process was initiated by a swarm of repeating earthquakes, prior to the M_L 4.0 event, which suggests aseismic slip and fits with the preslip model. Following the M_L4.0 event, the majority of its aftershocks, and the Mw 6.4 earthquake, were triggered by stress transfer, indicating a cascade triggering mechanism. Our observation suggests that the nucleation of the Mw 6.4 mainshock and its foreshocks can be jointly explained by the preslip and cascade models.

Acknowledgements

Waveform data were downloaded from the Incorporated Research Institutions for Seismology (IRIS) and the Southern California Earthquake Data Center. The HypoDD catalog can be accessed from Shelly (2020). Our foreshock catalog can be found in the supporting information. The maps in our paper were made using Generic Mapping Tools (Wessel et al., 2013) and MATLAB. We thank Katherine Scharer for sharing the surveyed surface ruptures. This work was co-supported by the National Natural Science Foundation of China (NSFC) under Grants 41874063 and U1939203, Shanghai Sheshan National Geophysical Observatory (No. 2020K02), the Fundamental Research Funds for the Central Universities of China (2-9-2019-172), and the Natural Sciences and Engineering Research Council of Canada Discovery Grant (RGPIN-2019-04297).

References

Abercrombie, R. E. (1996). The magnitude-frequency distribution of earthquakes recorded with deep seismometers at Cajon Pass, southern California. Tectonophysics, 261(1–3), 1–7. https://doi.org/10.1016/0040-1951(96)00052-2

Beroza, G. C., & Ellsworth, W. L. (1996). Properties of the seismic nucleation phase. *Tectonophysics*, *261*(1-3 SPEC. ISS.), 209–227. https://doi.org/10.1016/0040-1951(96)00067-4

Bouchon, M., H. Karabulut, M. Aktar, S. Ozalaybey, J. Schmittbuhl, and M. P. Bouin (2011), Extended nucleation of the 1999 M-w 7.6 Izmit earthquake, *Science, 331*(6019), 877–880, doi:10.1126/science.1197341.

Chen, K., Avouac, J. P., Aati, S., Milliner, C., Zheng, F., & Shi, C. (2020). Cascading and pulse-like ruptures during the 2019 Ridgecrest earthquakes in the Eastern California Shear Zone. *Nature Communications*, *11*, 22. https://doi.org/10.1038/s41467-019-13750-w

Chen, X., and P. M. Shearer (2013), California foreshock sequences suggest aseismic triggering process, *Geophysical Research Letters*, *40*, 2602–2607, doi:10.1002/grl.50444.

Crider, J. G., & Peacock, D. C. P. (2004). Initiation of brittle faults in the upper crust: A review of field observations. *Journal of Structural Geology*, *26*(4), 691–707. https://doi.org/10.1016/j.jsg.2003.07.007

Crotwell, H. P., Owens, T. J., & Ritsema, J. (1999). The TauP Toolkit: Flexible Seismic Travel-time and Ray-path Utilities. *Seismological Research Letters*, *70*(2), 154–160. https://doi.org/10.1785/gssrl.70.2.154

Dublanchet, P. (2018). The dynamics of earthquake precursors controlled by effective friction. *Geophysical Journal International*, *212*(2), 853–871.

Dodge, D. A., Beroza, G. C., & Ellsworth, W. L. (1996). Detailed observations of California foreshock sequences: Implications for the earthquake initiation process. *Journal of Geophysical Research: Solid Earth*, *101*(B10), 22371–22392. https://doi.org/10.1029/96jb02269

Ellsworth, W. L., & Beroza, G. C. (1995). Seismic evidence for an earthquake nucleation phase. *Science*, *268*(5212), 851–855. https://doi.org/10.1126/science.268.5212.851

Ellsworth, William L., & Bulut, F. (2018). Nucleation of the 1999 Izmit earthquake by a triggered cascade of foreshocks. *Nature Geoscience*, *11*(7), 531–535. https://doi.org/10.1038/s41561-018-0145-1

Felzer, K. R., R. E. Abercrombie, and G. Ekström (2004), A common origin for aftershocks, foreshocks, and multiplets, *Bulletin of the Seismological Society of America*, *94*(1), 88–99.

Gibbons, S. J., and F. Ringdal (2006), The detection of low magnitude seismic events using array-based waveform correlation, *Geophysical Journal International*, *165*, 149–166.

Goldberg, D. E., Melgar, D., Sahakian, V. J., Thomas, A. M., Xu, X., Crowell, B. W., & Geng, J. (2020). Complex Rupture of an Immature Fault Zone: A Simultaneous Kinematic Model of the 2019 Ridgecrest, CA Earthquakes. *Geophysical Research Letters*, *47*, e2019GL086382. https://doi.org/10.1029/2019GL086382

Helmstetter, A., and D. Sornette (2003), Importance of direct and indirect triggered seismicity in the ETAS model of seismicity, *Geophysical Research Letters, 30*(11), 1576, doi:10.1029/2003GL017670.

Kanamori, H., & Anderson, D. L. (1975). Theoretical basis of some empirical relations in seismology. *Bulletin of the Seismological Society of America*, *65*(5), 1073–1095.

Kato, A., J. Fukuda, T. Kumazawa, and S. Nakagawa (2016), Accelerated nucleation of the 2014 Iquique, Chile Mw 8.2 Earthquake, *Scientific Reports*, *6*, 24792, doi:10.1038/srep24792.

Kato, A., K. Obara, T. Igarashi, H. Tsuruoka, S. Nakagawa, and N. Hirata (2012), Propagation of slow slip leading up to the 2011 M w 9.0 Tohoku-Oki Earthquake, *Science*, *335*, 705–708, doi:10.1126/science.1215141.

Kendrick, K. J., Akciz, S. O., Angster, S. J., Avouac, J., Bachhuber, J. L., Bennett, S. E., Blake, K., Bork, S., Brooks, B. A., Burgess, P., Chupik, C., Dawson, T., DeFrisco, M. J., Delano, J., DeLong, S., Dolan, J. F., DuRoss, C. B., Ericksen, T., Frost, M. E. (2019). Geologic observations of surface fault rupture associated with the Ridgecrest M6.4 and M7.1 earthquake sequence by the Ridgecrest Rupture Mapping Group. In *2019 SCEC Annual Meeting* (p. Poster #217).

Lin, J., & Stein, R. S. (2004). Stress triggering in thrust and subduction earthquakes and stress interaction between the southern San Andreas and nearby thrust and strike-slip faults. *Journal of Geophysical Research: Solid Earth*, *109*(B2), 1–19. https://doi.org/10.1029/2003jb002607

Liu, M., Zhang, M., Zhu, W., Ellsworth, W. L., & Li, H. (2020). Rapid Characterization of the July 2019 Ridgecrest, California, Earthquake Sequence From Raw Seismic Data Using Machine-Learning Phase Picker. *Geophysical Research Letters*, *47*, e2019GL086189. https://doi.org/10.1029/2019GL086189

Manighetti, I., Campillo, M., Bouley, S., & Cotton, F. (2007). Earthquake scaling, fault segmentation, and structural maturity. *Earth and Planetary Science Letters*, *253*(3–4), 429–438. https://doi.org/10.1016/j.epsl.2006.11.004

McGuire, J. J., M. Boettcher, and T. H. Jordan (2005), Foreshock sequences and short-term earthquake predictability on East Pacific Rise transform faults, *Nature*, *434*, 457– 461, doi:10.1038/nature03377.

McLaskey, G. C. (2019). Earthquake Initiation From Laboratory Observations and Implications for Foreshocks. *Journal of Geophysical Research: Solid Earth*, *124*, 12882–12904. https://doi.org/10.1029/2019JB018363

McLaskey, G. C., and D. A. Lockner (2014), Preslip and cascade processes initiating laboratory stick–slip, *Journal of Geophysical Research: Solid Earth*, *119*, 6323–6336, doi:10.1002/2014JB011220.

Mignan, A. (2014). The debate on the prognostic value of earthquake foreshocks: A meta-analysis. *Scientific Reports*, *4*, 4099. https://doi.org/10.1038/srep04099

Noda, H., M. Nakatani, and T. Hori (2013), Large nucleation before large earthquakes is sometimes skipped due to cascade-up - Implications from a rate and state simulation of faults with hierarchical asperities, *Journal of Geophysical Research: Solid Earth*, *118*, 2924–2952, doi:10.1002/jgrb.50211.

Perrin, C., Manighetti, I., Ampuero, J. P., Cappa, F., & Gaudemer, Y. (2016). Location of largest earthquake slip and fast rupture controlled by along-strike change in fault structural maturity due to fault growth. *Journal of Geophysical Research: Solid Earth*, *121*(5), 3666–3685. https://doi.org/10.1002/2015JB012671

Press, W., B. Flannery, S. Teukolsky, and W. Vetterling (1986), Numerical Recipes, *Cambridge Univ*. Press, Cambridge.

Ross, Z. E., Idini, B., Jia, Z., Stephenson, O. L., Zhong, M., Wang, X., et al. (2019). Hierarchical interlocked orthogonal faulting in the 2019 Ridgecrest earthquake sequence. *Science*, *366*(6463), 346–351. https://doi.org/10.1126/science.aaz0109

Savage, H. M., Keranen, K. M., P. Schaff, D., & Dieck, C. (2017). Possible precursory signals in damage zone foreshocks. *Geophysical Research Letters*, *44*, 5411–5417. https://doi.org/10.1002/2017GL073226

Shelly, D. R. (2020). A High-Resolution Seismic Catalog for the Initial 2019 Ridgecrest Earthquake Sequence: Foreshocks, Aftershocks, and Faulting Complexity. *Seismological Research Letters*, *91*(4), 1971-1978. https://doi.org/10.1785/0220190309

Tape, C., Holtkamp, S., Silwal, V., Hawthorne, J., Kaneko, Y., Ampuero, J. P., et al. (2018). Earthquake nucleation and fault slip complexity in the lower crust of central Alaska. *Nature Geoscience*, *11*, 536-541. https://doi.org/10.1038/s41561-018-0144-2

Thomas, A. M., Bürgmann, R., & Dreger, D. S. (2013). Incipient faulting near lake pillsbury, california, and the role of: Accessory faults in plate boundary evolution. *Geology*, *41*(10), 1119–1122. https://doi.org/10.1130/G34588.1

Toda, S., Stein, R. S., Richards-Dinger, K., & Bozkurt, S. B. (2005). Forecasting the evolution of seismicity in southern California: Animations built on earthquake stress transfer. *Journal of Geophysical Research: Solid Earth*, *110*, B05S16. https://doi.org/10.1029/2004JB003415

Uchida, N. (2019). Detection of repeating earthquakes and their application in characterizing slow fault slip. *Progress in Earth and Planetary Science*, *6*, 40.

Uchida, N., & Bürgmann, R. (2019). Repeating earthquakes. *Annual Review of Earth and Planetary Sciences*, *47*(1). https://doi.org/10.1146/annurev-earth-053018-060119

Wesnousky, S. G. (1988). Seismological and structural evolution of strike-slip faults. *Nature*, *335*(6188), 340-343. https://doi.org/10.1038/335340a0

Wessel, P., Smith, W. H. F., Scharroo, R., Luis, J., & Wobbe, F. (2013). Generic mapping tools: Improved version released. *Eos*, *94*(45), 409–410. https://doi.org/10.1002/2013EO450001

Xu, Y., & Wen, L. (2019). Relative directivity inversion of small earthquake rupture. *Geophysical Journal International*, *218*(1), 631–639. https://doi.org/10.1093/gji/ggz179

Yang, J., Zhu, H., & Lumley, D. (2020). Time-Lapse Imaging of Coseismic Ruptures for the 2019 Ridgecrest Earthquakes Using Multiazimuth Backprojection With Regional Seismic Data and a 3-D Crustal Velocity Model. *Geophysical Research Letters*, 47(9), e2020GL087181.

Yao, D., Huang, Y., Peng, Z., & Castro, R. R. (2020). Detailed Investigation of the Foreshock Sequence of the 2010 Mw 7.2 El Mayor-Cucapah Earthquake. *Journal of Geophysical*

Research: Solid Earth, *124*, e2019JB019076 https://doi.org/10.1029/2019JB019076

Yoon, C. E., Yoshimitsu, N., Ellsworth, W. L., & Beroza, G. C. (2019). Foreshocks and Mainshock Nucleation of the 1999 M w 7.1 Hector Mine, California, Earthquake. *Journal of Geophysical Research: Solid Earth*, *124*(2), 1569–1582. https://doi.org/10.1029/2018JB016383

Zhang, M., & Wen, L. (2015a). An effective method for small event detection: match and locate (M&L). *Geophysical Journal International*, *200*(3), 1523–1537. https://doi.org/10.1093/gji/ggu466

Zhang, M., & Wen, L. (2015b). Seismological evidence for a low-yield nuclear test on 12 May 2010 in North Korea. *Seismological Research Letters*, *86*(1), 138–145. https://doi.org/10.1785/02201401170

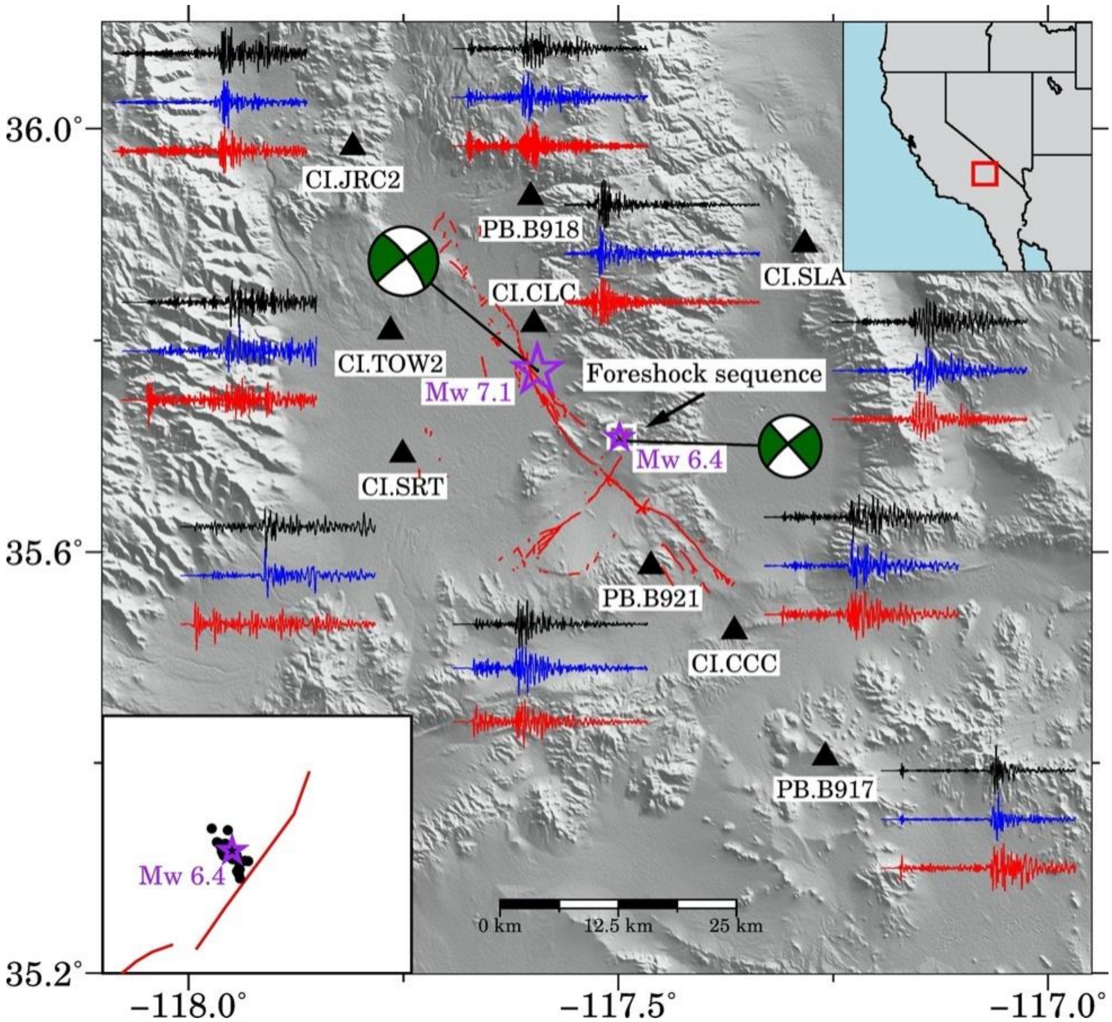

Figure 1. Map view of the study region. Epicenters and focal mechanisms of the Mw 6.4 and Mw 7.1 earthquakes are indicated by purple stars and beach balls, respectively. Black triangles denote the seismic stations used in this study. Red lines mark the surveyed surface ruptures (Kendrick et al., 2019). Three-component seismograms of the template event are plotted close to their corresponding stations. (left bottom inset) The 40 identified foreshocks, along with the Mw 6.4 mainshock, are shown in the zoomed-in area (white rectangle in main figure). The top-right displays a regional map of the United States, with the red rectangle indicating the study region.

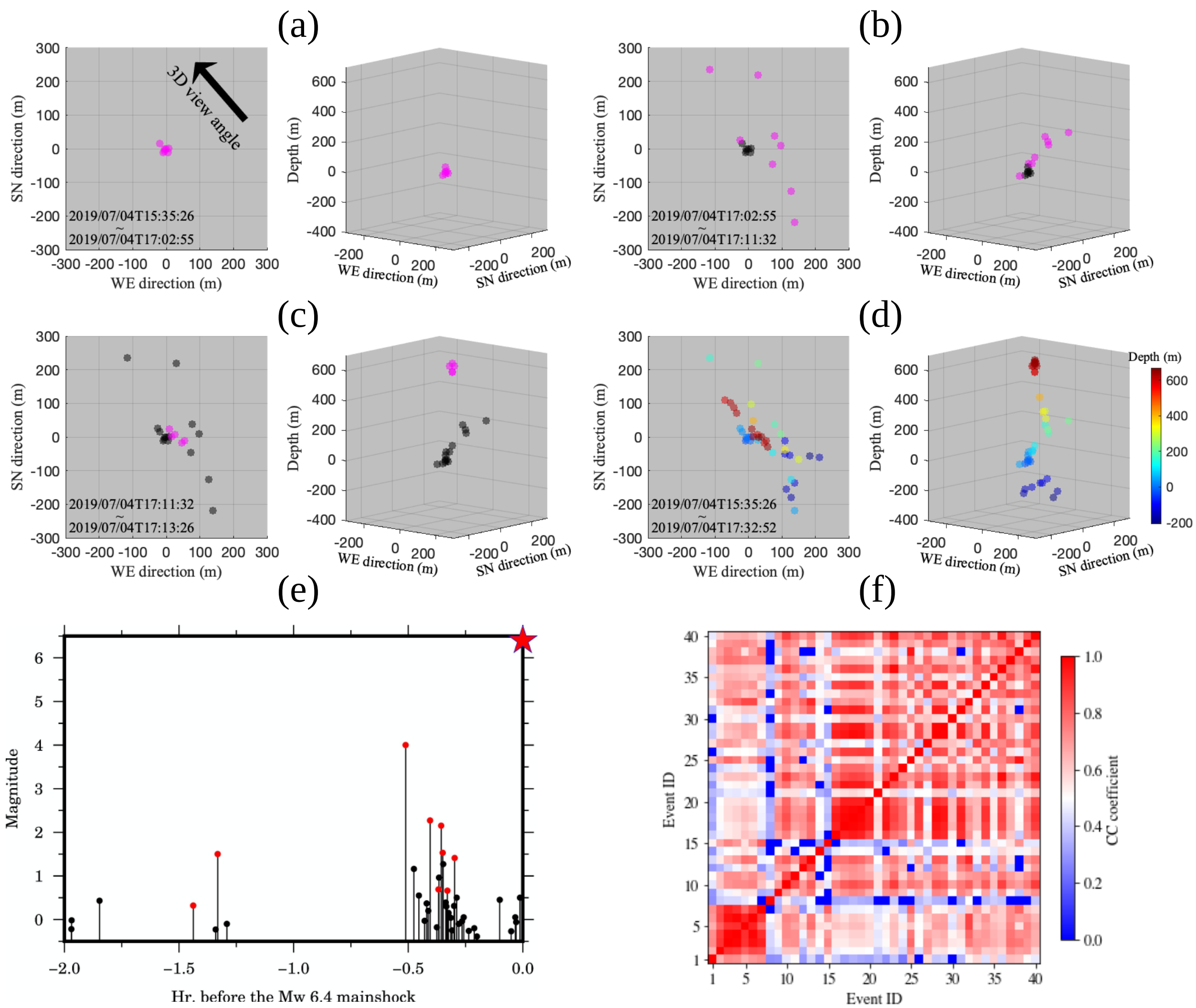

Figure 2. Detailed spatial-temporal evolution of foreshocks and their waveform similarity analysis. (a) Left panel shows the map-view epicenters of foreshocks (purple dots) that occurred on July 4, 2019, from 15:35:25 to 17:02:55 (UTC; EQ 1-7). The right panel displays a 3D view, with a view angle indicated by the black arrow in the left panel. All event locations are relative to the hypocenter of the template event. (b) Similar to (a), but for the foreshocks that occurred from 17:02:55 to 17:11:32 (UTC; EQ 8-15). Black dots represent events that occurred within the previous time window. (c) Similar to (b), but for the foreshocks that occurred from 17:11:32 to 17:13:26 (UTC; EQ 16-20). (d) All foreshocks that occurred before the Mw 6.4 mainshock, colored by depth. (e) Magnitude-time distribution of the foreshocks in our catalog (dots), along with the Mw 6.4 event (red star). Red dots indicate events that are only cataloged by the SCSN.

(f) Pairwise CC coefficients for 40 foreshocks. Event IDs are ordered by their origin time (see Table S1).

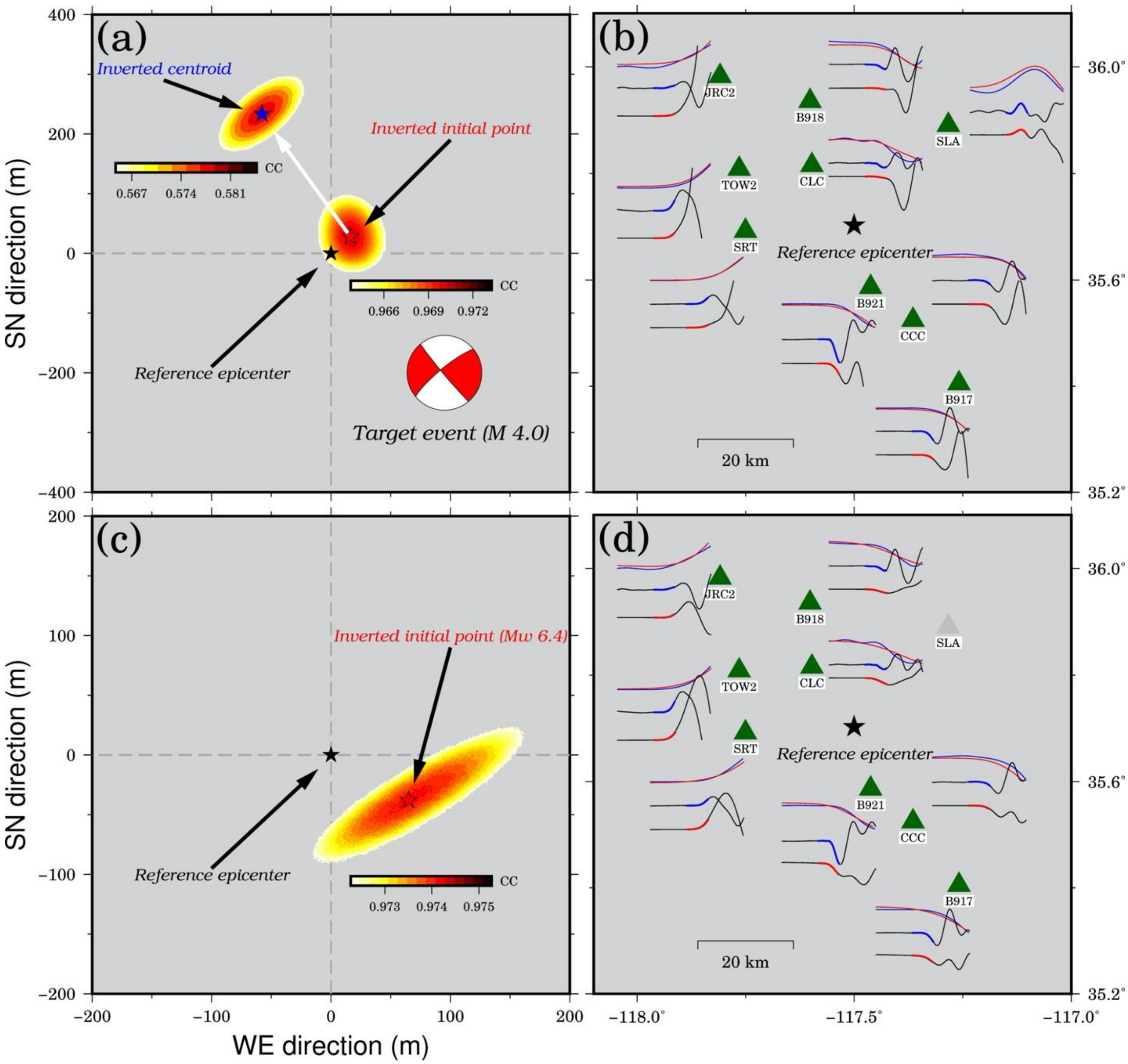

Figure 3. Rupture directivity analysis of the M_L 4.0 event and the initial rupture point of the Mw 6.4 mainshock determined by the M&L method. (a) Rupture directivity (white arrow) of the M_L 4.0 event. The black star indicates the epicenter of the reference event. Red and blue stars represent the initial rupture point and centroid point of the M_L 4.0 foreshock, respectively. The distributions of their averaged CC coefficients are shown with the corresponding color bars. Beach ball shows the focal mechanism solution of the M_L 4.0 event (SCSN). All locations are

relative to the epicenter of the master event, in meters. (b) Initial P phase comparison between the M_L 4.0 event (red) and the M_L 1.5 reference event (blue) after travel time correction by M&L, which is used for the initial rupture point determination of the M_L 4.0 event. Initial P phases are plotted along with their early P phases over an extended time window (bottom two traces). Dark-green triangles represent the stations used for location determination by the M&L method. (c) Similar to (a), but for the initial rupture point determination of the Mw 6.4 mainshock. (d) Similar to (b), but for the initial rupture point determination of the Mw 6.4 mainshock. Gray triangle represents the discarded station.

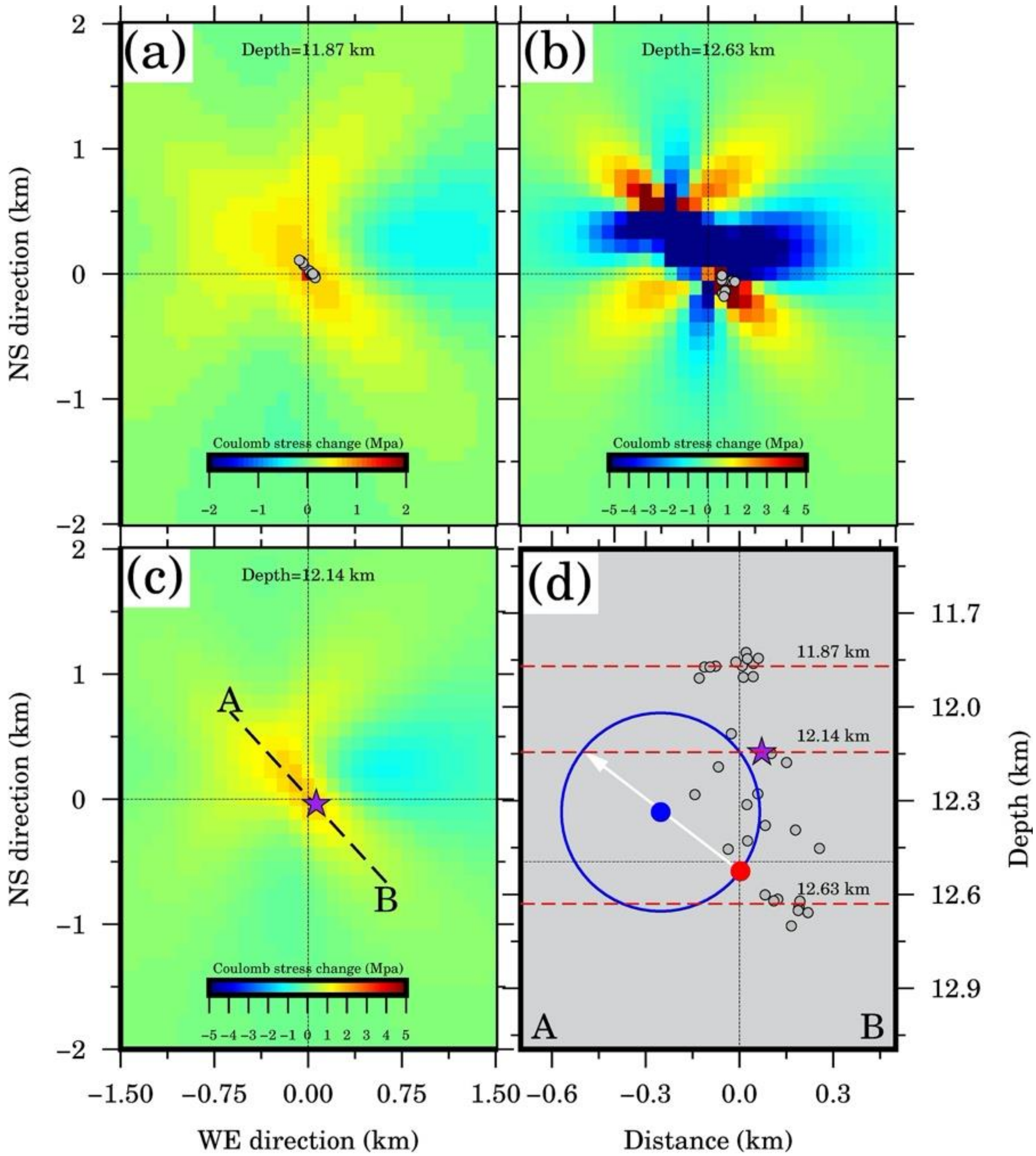

Figure 4. Earthquake triggering mechanism following the M_L 4.0 event. (a) Coulomb stress change imparted by the M_L 4.0 earthquake at a depth of 11.87 km. Event epicenters (gray dots) are relative to the epicenter of the M_L 1.5 master event. (b) Similar to (a), but for the seismicity at a depth of 12.63 km. (c) Similar to (a), but for the depth of the initial rupture point of the Mw 6.4 mainshock (12.14 km). The purple star shows the epicenter of the initial rupture point of the Mw 6.4 mainshock. (d) Cross-section of the foreshock distribution along the strike direction of the M_L 4.0 event (A–B in (c)). The blue circle represents the possible rupture region of the M_L 4.0 foreshock inferred from twice the distance between its initial rupture point (red dot) and

centroid point (blue dot). The purple star shows the initial rupture point of the Mw 6.4 mainshock. Gray dots represent the hypocenters of events that occurred after the M_L 4.0 event and before the Mw 6.4 mainshock. The three red dashed lines mark the depths shown in Figures 4a-c.

Geophysical Research Letters

Supporting Information for

Detailed nucleation process and mechanism of the July 2019 Mw 6.4 Ridgecrest, California earthquake

Min Liu[1,2], Miao Zhang[2*] and Hongyi Li[1*,3]

[1]School of Geophysics and Information Technology, China University of Geosciences (Beijing), Beijing, China
[2]Department of Earth and Environmental Sciences, Dalhousie University, Halifax, Nova Scotia, Canada
[3]Shanghai Sheshan National Geophysical Observatory, Shanghai, China

Corresponding author: Miao Zhang (miao.zhang@dal.ca) and Hongyi Li (lih@cugb.edu.cn)

Contents of this file:

Additional Supporting Information (Files uploaded separately)

Introduction

This supporting information provides two texts, 43 figures, one table (separate from this file) and one movie (separate from this file) to support the discussions in the main text.

Text S1. Earthquake locaiton uncertainty

Location uncertainty is essential for evaluating the confidence of earthquake locations. However, there is no standard method for assessing the uncertainty of locations obtained with waveform-based methods. To estimate the location uncertainty of foreshocks listed in the Match&Locate (M&L) catalog, we conducted a bootstrapping analysis for the two detections with the highest and lowest averaged cross-correlation (CC) values (EQ 3 with CC of 0.8851 and EQ 30 with CC of 0.3635; See event ID in Table S1), which roughly represent the best and worst location results, respectively. The principle is to repeatedly perform the M&L relocation and remove one phase (P or S) recorded at one three-component station in each round. We adopted nine stations (18 phases and 54 components) in the M&L relocation, which means the M&L relocation was repeated 18 times, with one phase removed each time. The detailed procedure was the same as step 2 of the foreshock catalog creation (see Section 2 in the main text). The results of the bootstrapping analysis indicate that the event with the highest CC value has a location uncertainty of approximately 3 m, both horizontally and vertically, and the event with the lowest CC value has a slightly larger location uncertainty, of 8 m horizontally and 10 m vertically (Figure S4). We assumed the location uncertainty of the other foreshocks was within the range of these two events. Thus, our horizontal and vertical location uncertainties are 3–8 m and 3–10 m, respectively.

Following Zhang and Wen (2015a), we show the plan-view CC convergence and waveform comparison between each event with the template event (M_L 1.5) after relatively travel-time correction based on their location difference (Figure S5-43).

Text S2. Estimation of rupture radius from local magnitude

We estimated the rupture dimensions for the M_L1.5 and M_L 2.15 events based on their local magnitude (M_L) and a simple circular crack model. We first converted the M_L to the scalar moment (M_0) based on the moment-magnitude relationship (Abercrombie, 1996) in the region, as below:

$$\log(M_0) = 9.8 + M_L \qquad (1)$$

We then estimated the rupture radius r from M_0, based on a simple circular crack model and the scaling relationship proposed by Kanamori & Anderson (1975) :

$$r = \left(\frac{7M_0}{16\Delta\sigma}\right)^{1/3} \qquad (2)$$

Here, an empirical stress drop ($\Delta\sigma$) of 3 MPa was adopted in the calculation of the rupture radius (Yoon et al., 2019). Thus, the rupture radiuses of the M_L1.5 and M_L 2.15 events were 31 m and 50 m, respectively.

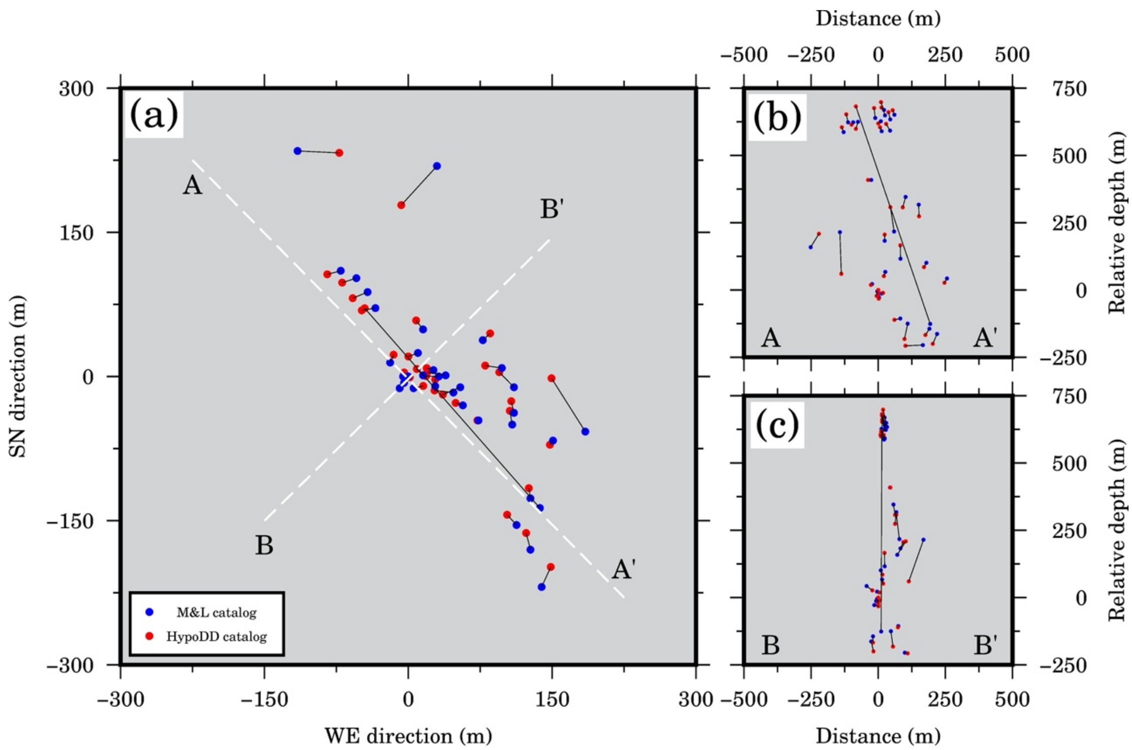

Figure S1. (a) Plan-view comparison of locations of the 35 foreshocks common to both the M&L catalog (blue dots) and the hypoDD catalog (red dots). Event locations are relative to the hypocenter of the M_L 1.5 event. The corresponding event-pairs in the two catalogs are connected by black lines. (b) Similar to (a), but for the cross-section along AA', which corresponds to one of the fault planes of the M_L 4.0 foreshock. (c) Similar to (b), but for the cross-section along BB'. The event-pair with a large location difference is further analyzed in Figure S2.

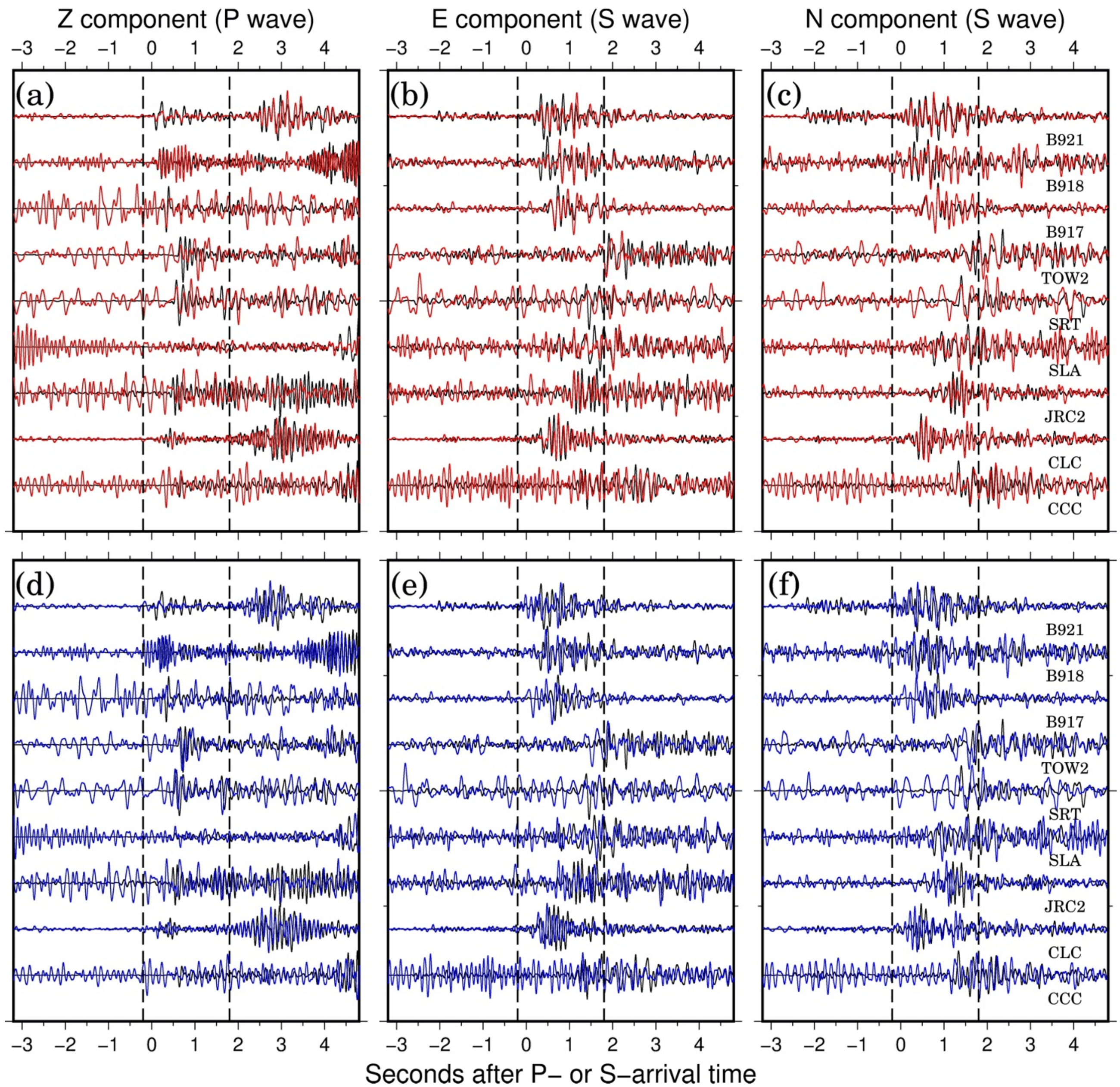

Figure S2. Investigation of the location reliability for the event pair with large location difference in Figure S1 (see main text). We allocated the corresponding locations and origin times, listed in the M&L and hypoDD catalogs, to the event, and compared its waveforms with the M_L 1.5 event after location correction. (a–c) Red and black waveforms represent the three-component seismograms of the event located by M&L and the reference event (M_L 1.5), respectively. The two black dashed lines highlight the template windows used in the M&L method. (d-f) Similar to (a–c), but for the hypoDD location. Clearly, the event was mislocated in the hypoDD catalog.

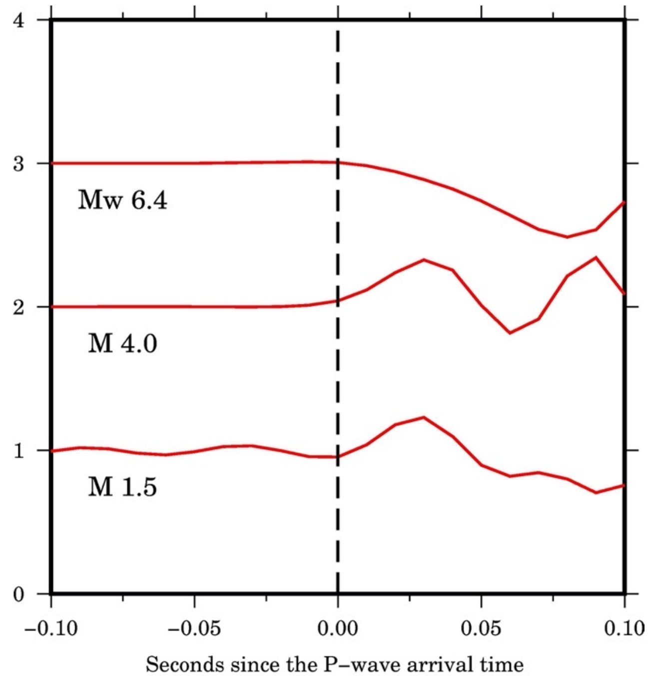

Figure S3. Comparison of the early P phases between the M_L 1.5, M_L 4.0 foreshocks, and the Mw 6.4 mainshock. All traces were aligned at the manual P first arrivals.

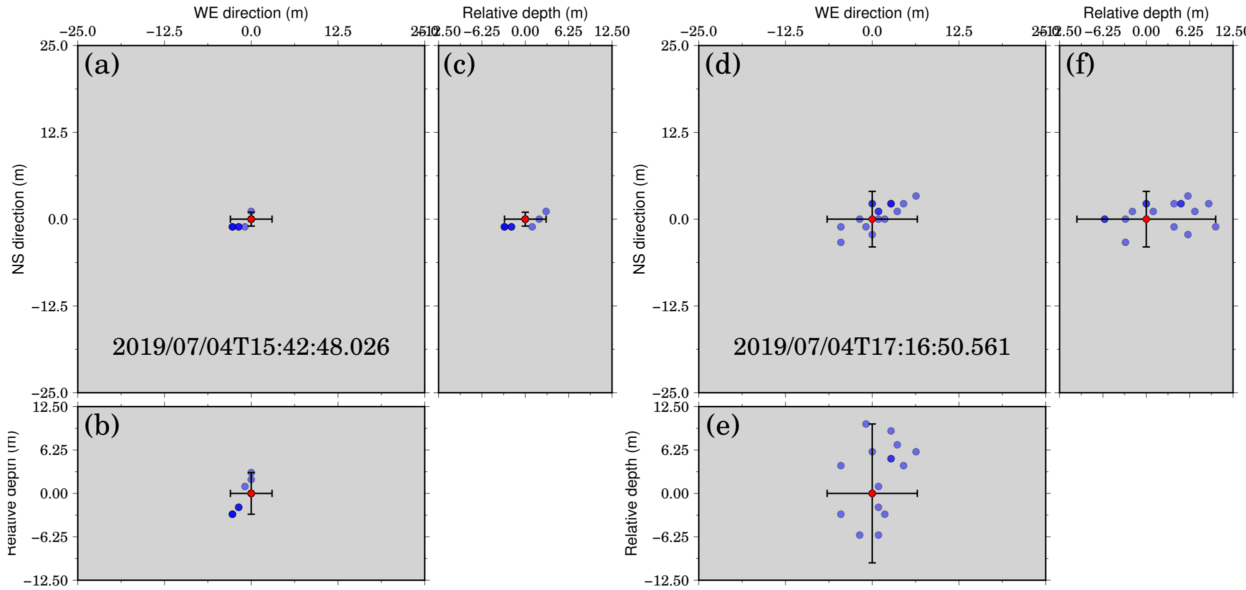

Figure S4. Location uncertainty of the two events with the highest and lowest CC values. (a) Red diamonds represent the epicentral location of the event located with the M&L method with the highest CC value (EQ 3 with a CC of 0.8851; See event ID in Table S1). Blue dots indicate the relocations based on the bootstrapping analysis. Blueness is proportional to the number of overlapping locations. The black error bar indicates the horizontal location uncertainty revealed by the bootstrapping analysis. (b–c) Similar to (a) but for the two cross-sections along the WE and NS directions. Black error bars represent the vertical location uncertainty. (d-e) Similar to (a-c) but for the event with the lowest CC value (EQ 30 with CC of 0.3635; See event ID in Table S1).

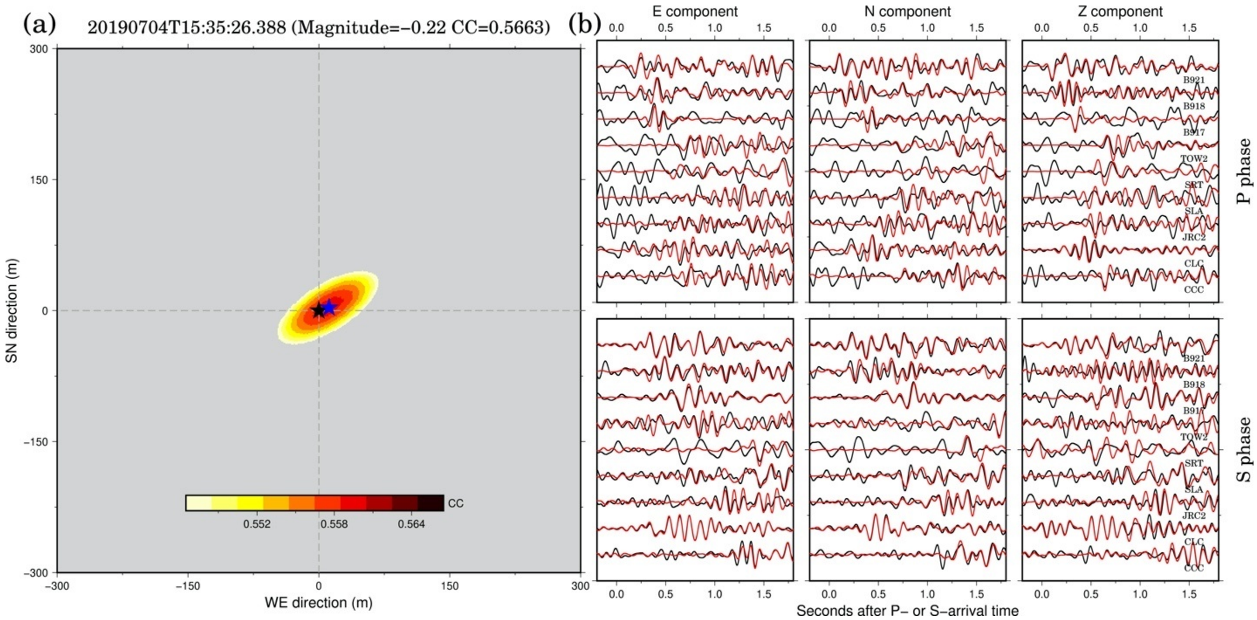

Figures S5. Horizontal CC convergence of EQ 1 (see event ID in Table S1) and its waveform comparison with the template event (M_L 1.5). (a) Black and blue stars represent the epicenters of the template and detected events, respectively. The distribution of averaged CC coefficients is shown with a color bar. (b) Waveform comparison of P phases (top panel) and S phases (bottom panel) between EQ 1 (red) and template (black) event, from nine three-component stations after relative travel time correction.

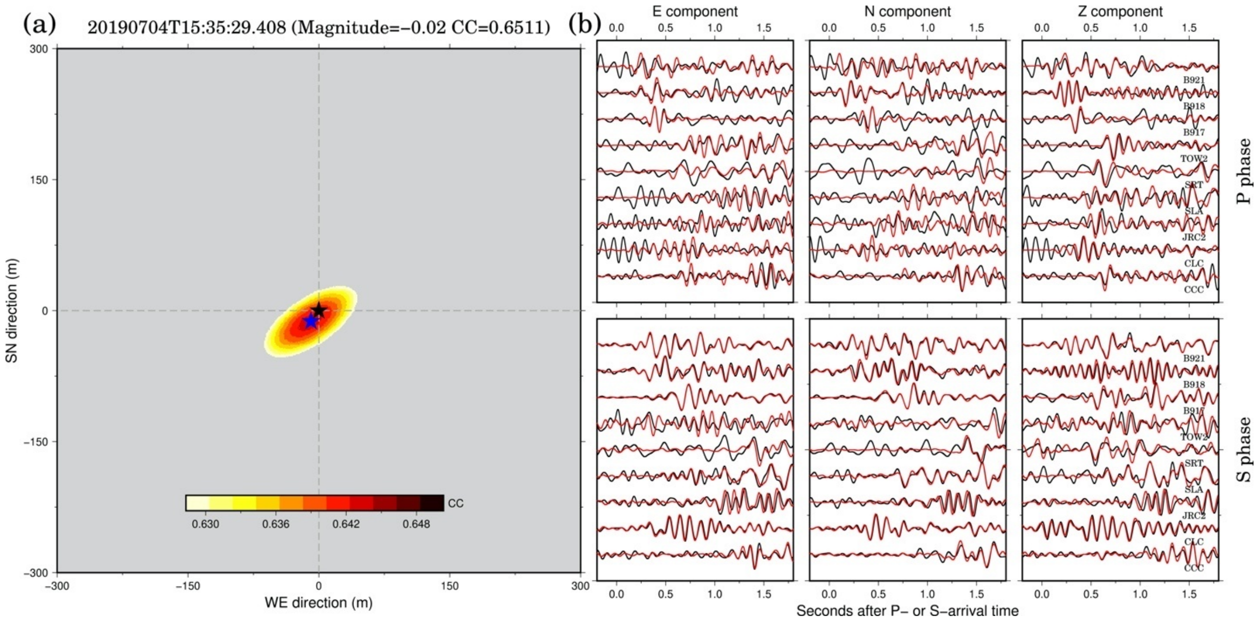

Figures S6. Smilar to Figure S5, but for EQ 2.

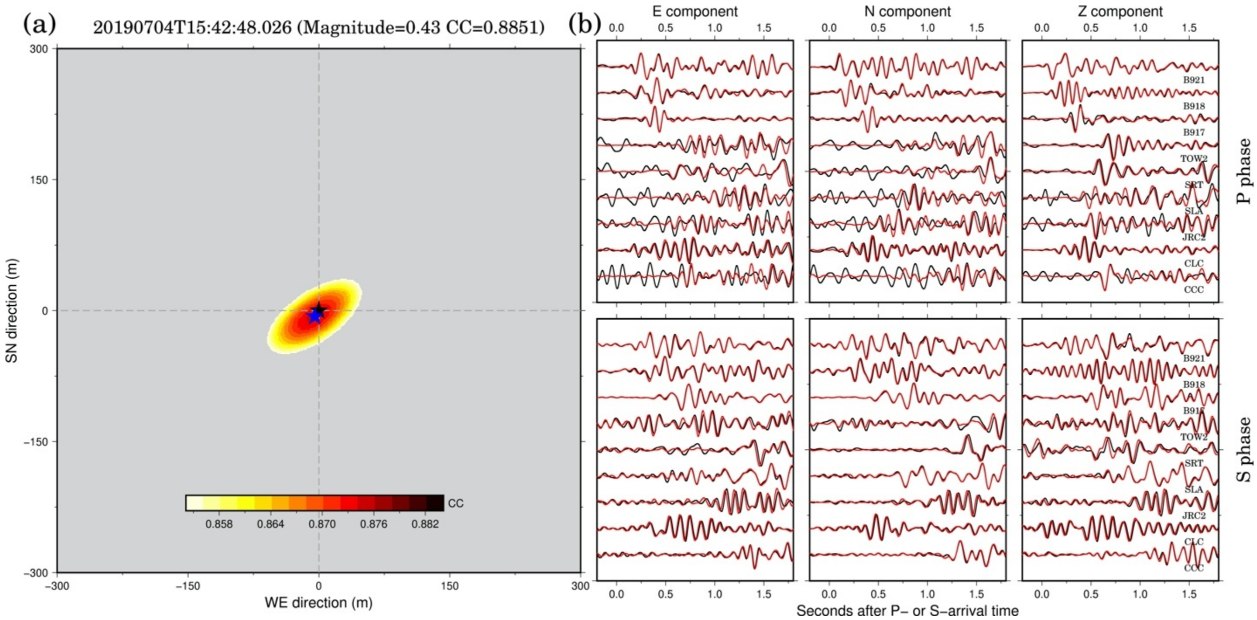

Figures S7. Smilar to Figure S5, but for EQ 3.

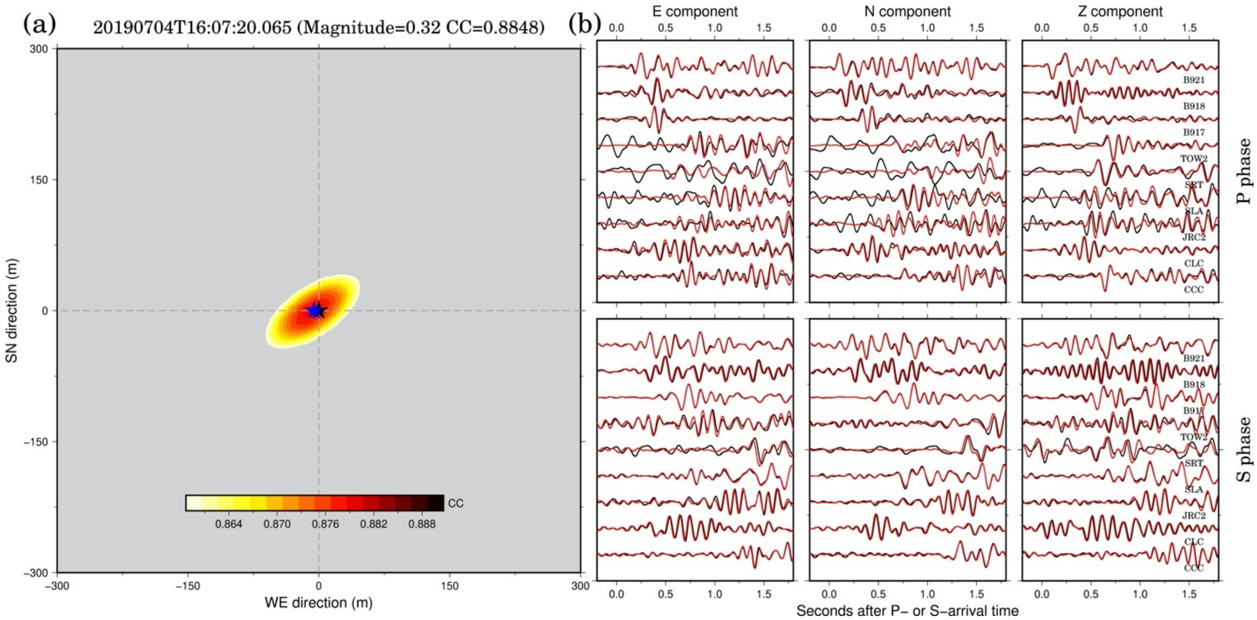

Figures S8. Smilar to Figure S5, but for EQ 4.

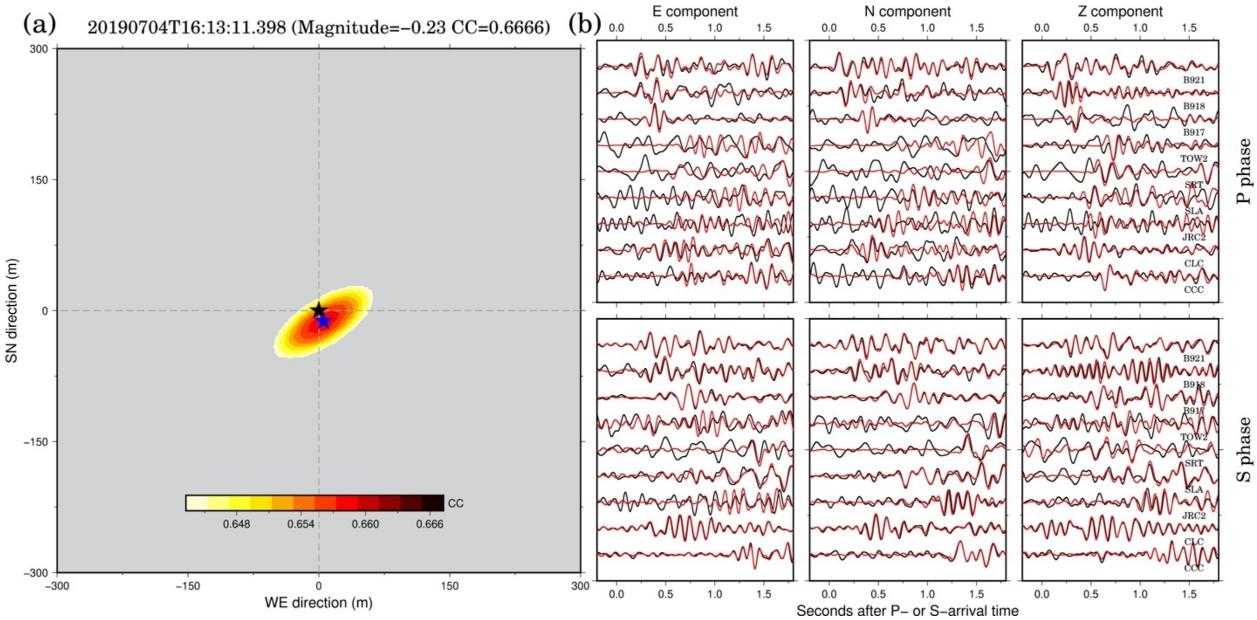

Figures S9. Smilar to Figure S5, but for EQ 5.

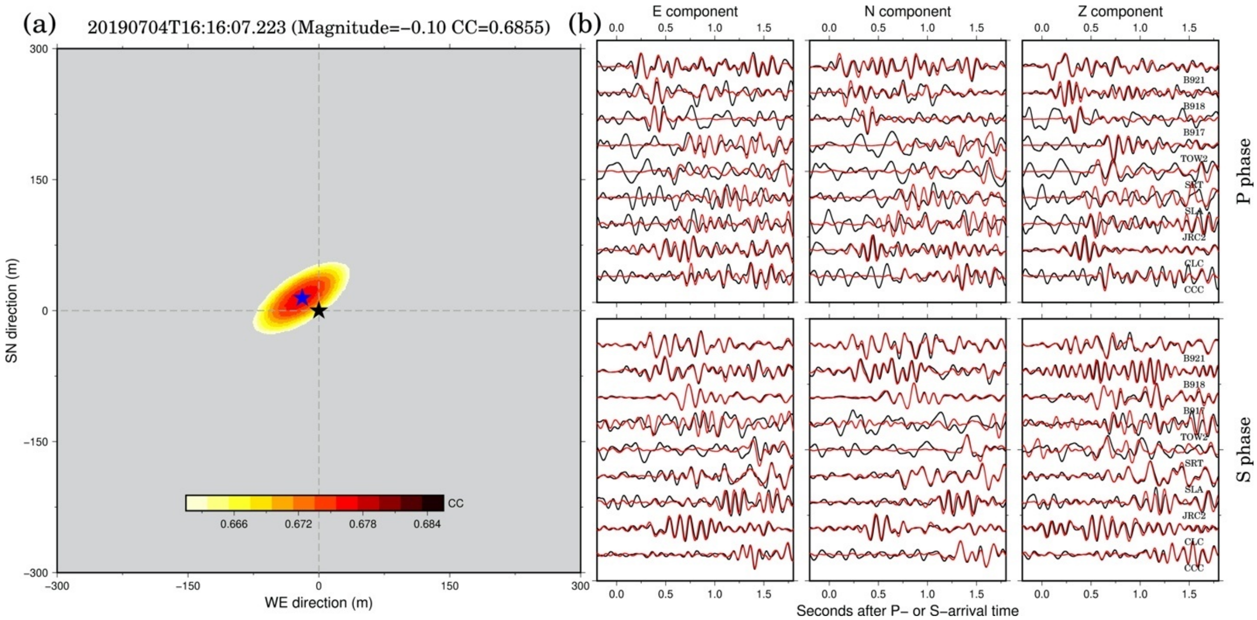

Figures S10. Smilar to Figure S5, but for EQ 7.

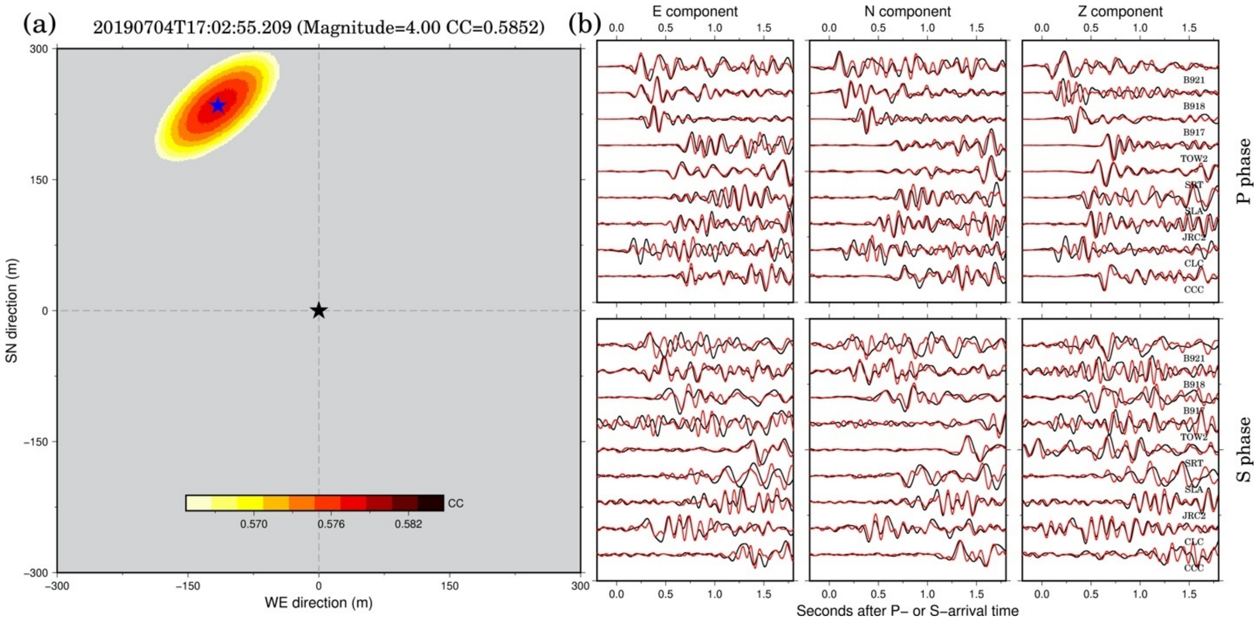

Figures S11. Smilar to Figure S5, but for EQ 8.

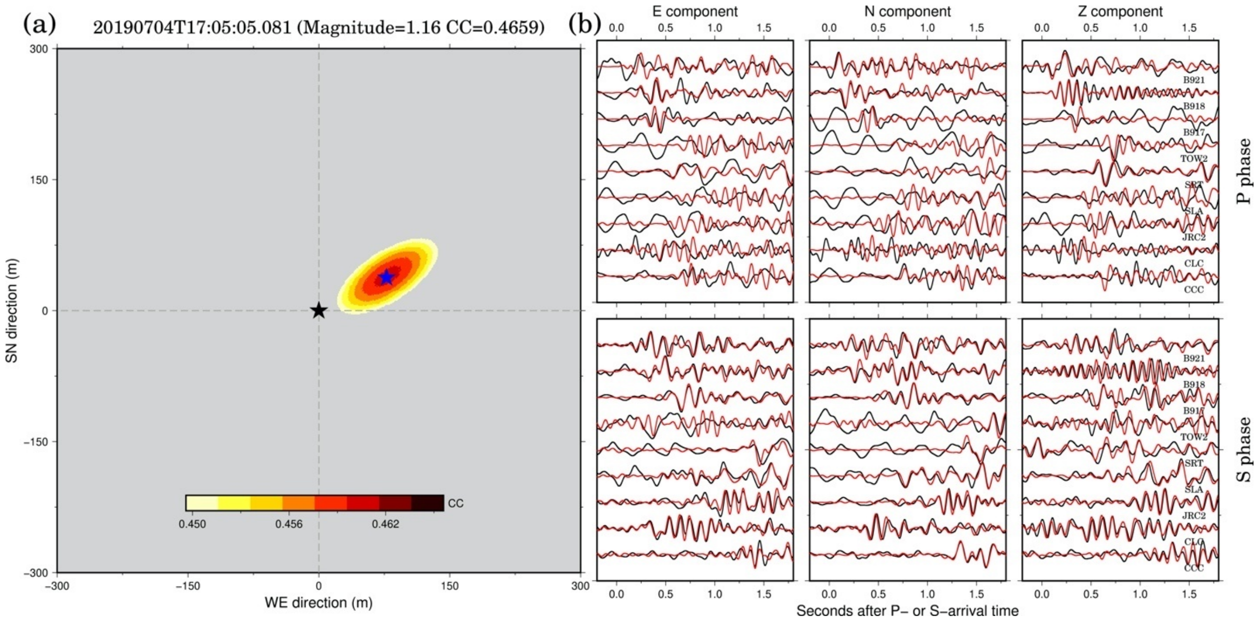

Figures S12. Smilar to Figure S5, but for EQ 9.

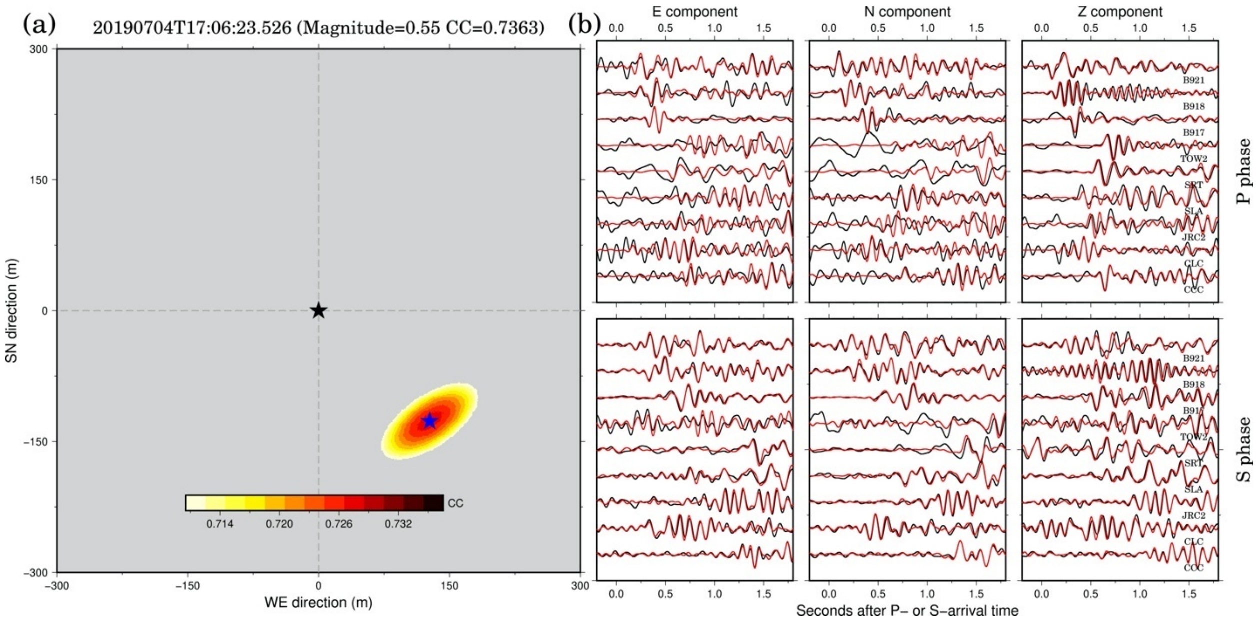

Figures S13. Smilar to Figure S5, but for EQ 10.

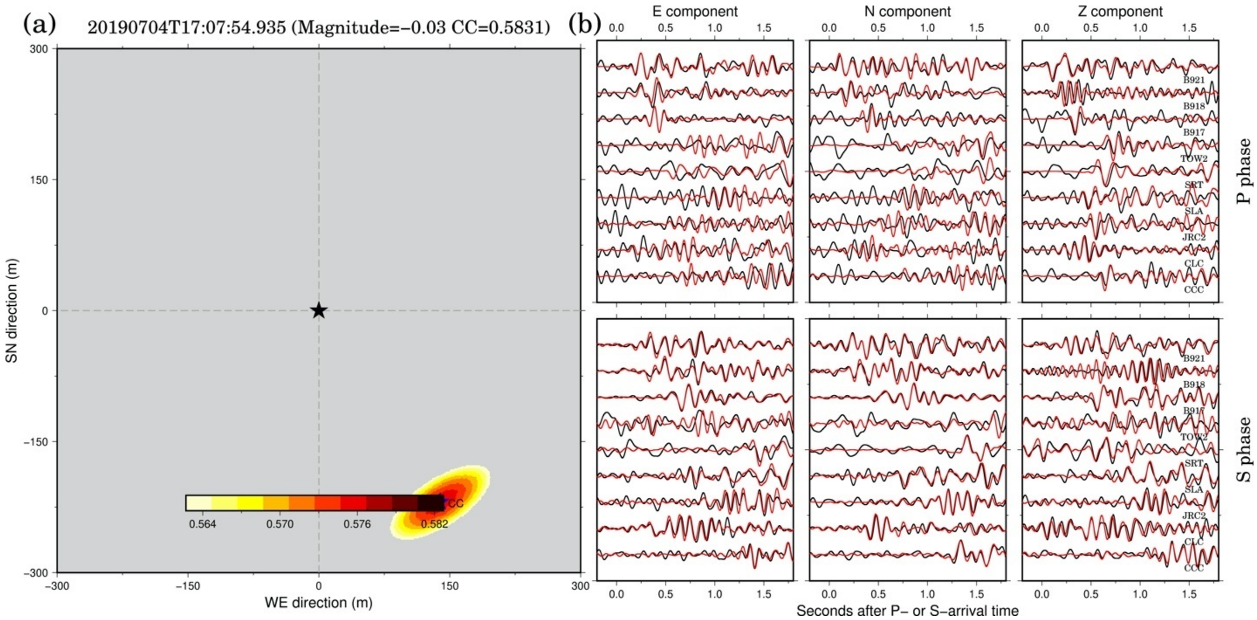

Figures S14. Smilar to Figure S5, but for EQ 11.

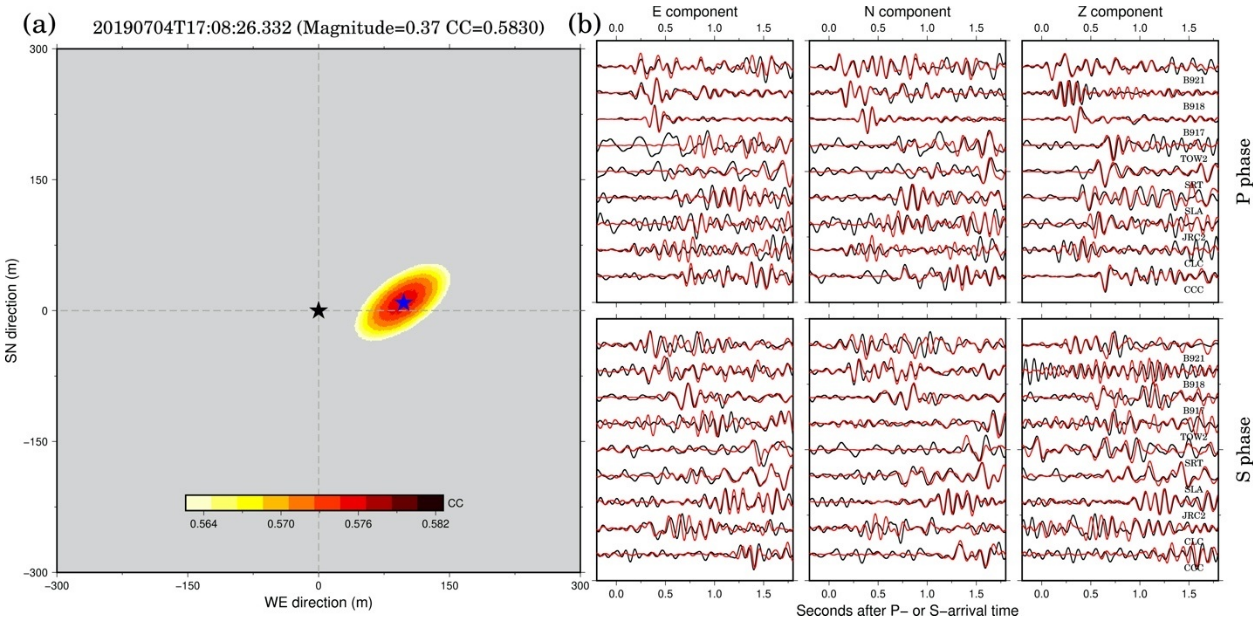

Figures S15. Smilar to Figure S5, but for EQ 12.

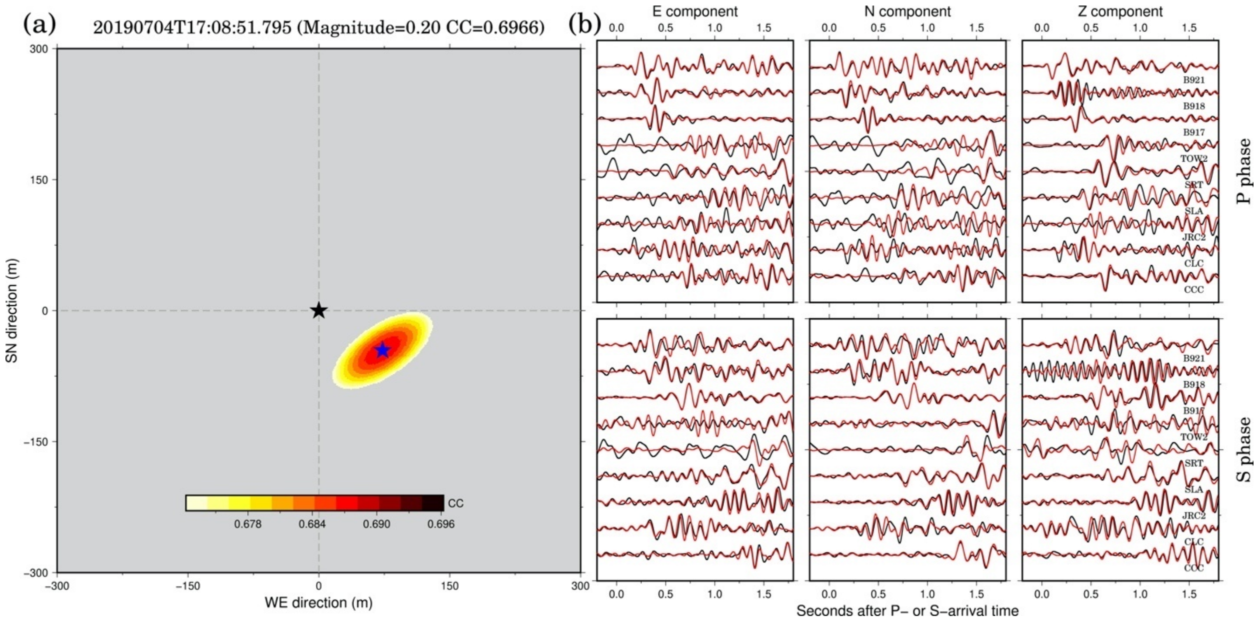

Figures S16. Smilar to Figure S5, but for EQ 13.

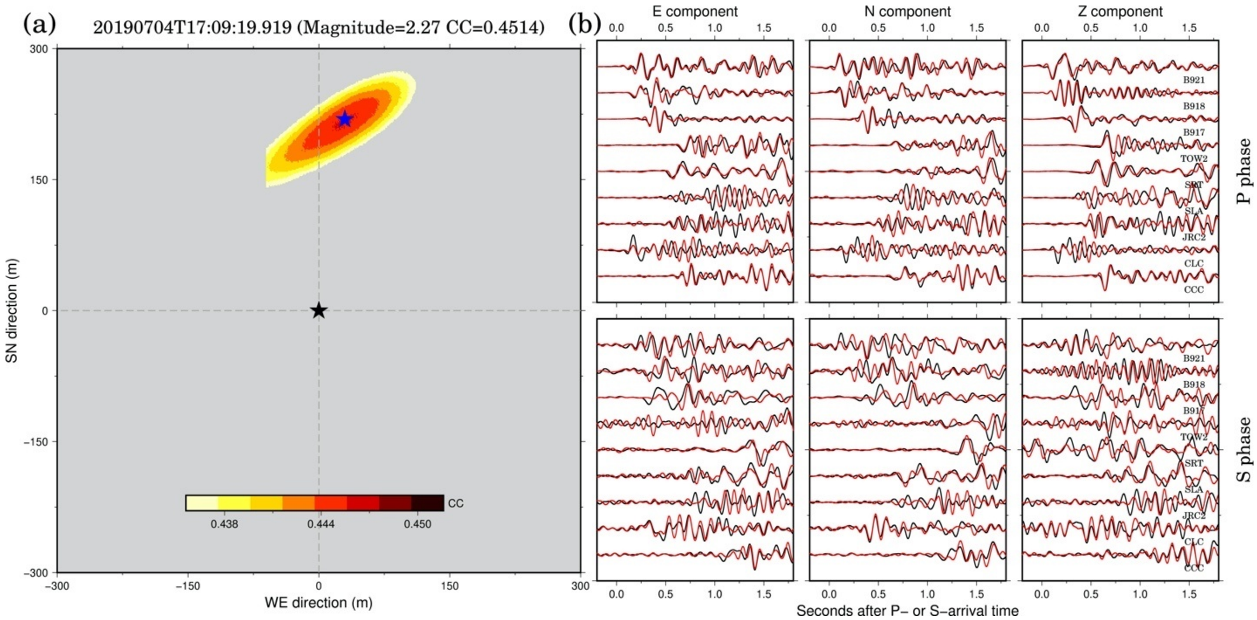

Figures S17. Smilar to Figure S5, but for EQ 14.

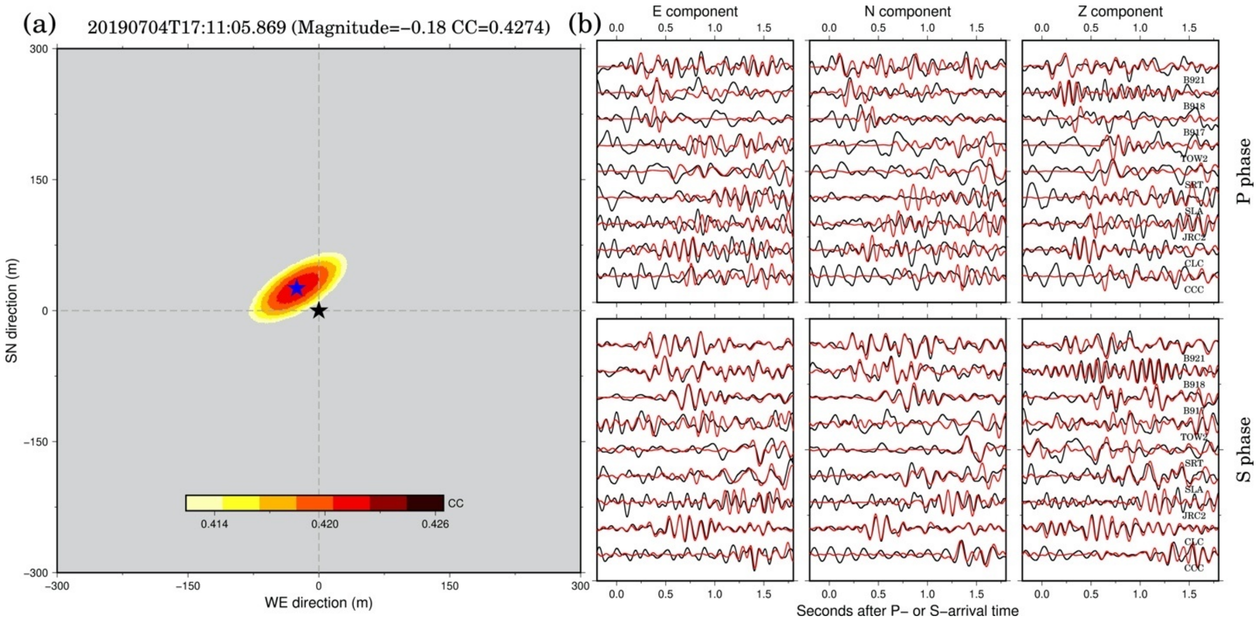

Figures S18. Smilar to Figure S5, but for EQ 15.

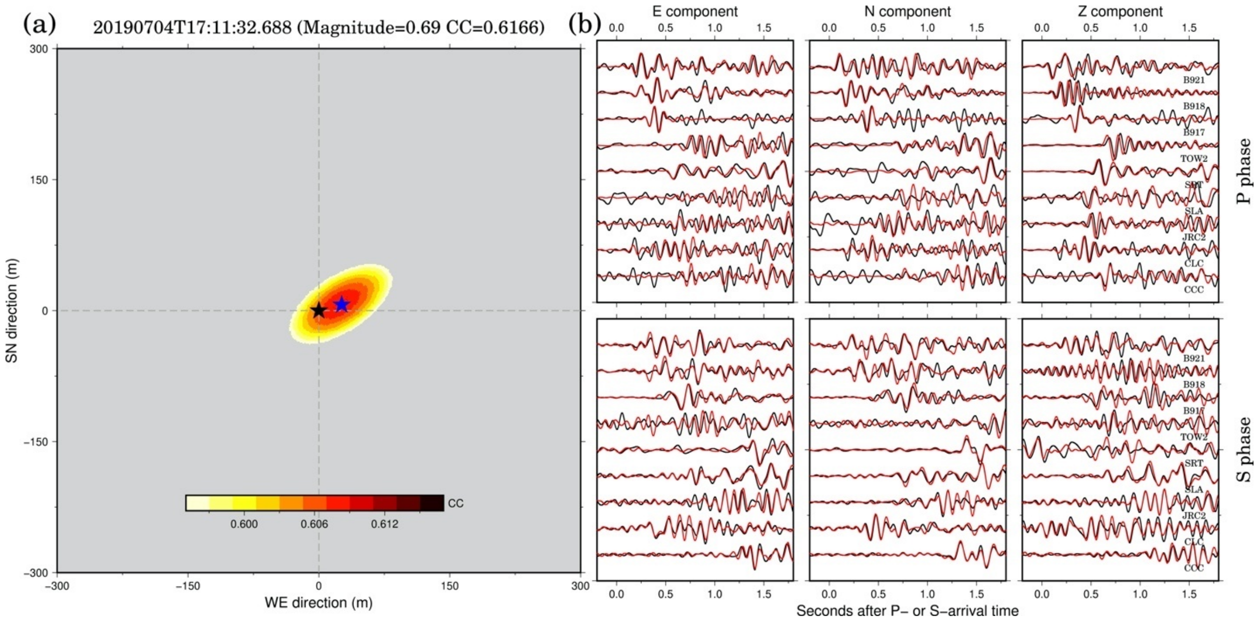

Figures S19. Smilar to Figure S5, but for EQ 16.

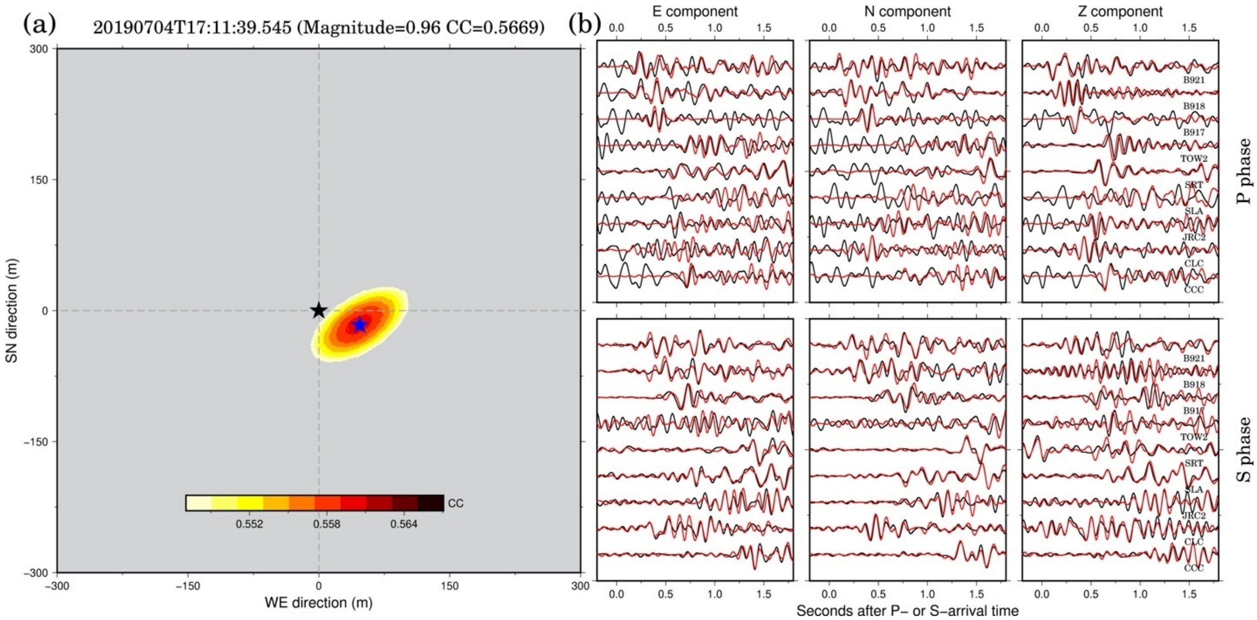

Figures S20. Smilar to Figure S5, but for EQ 17.

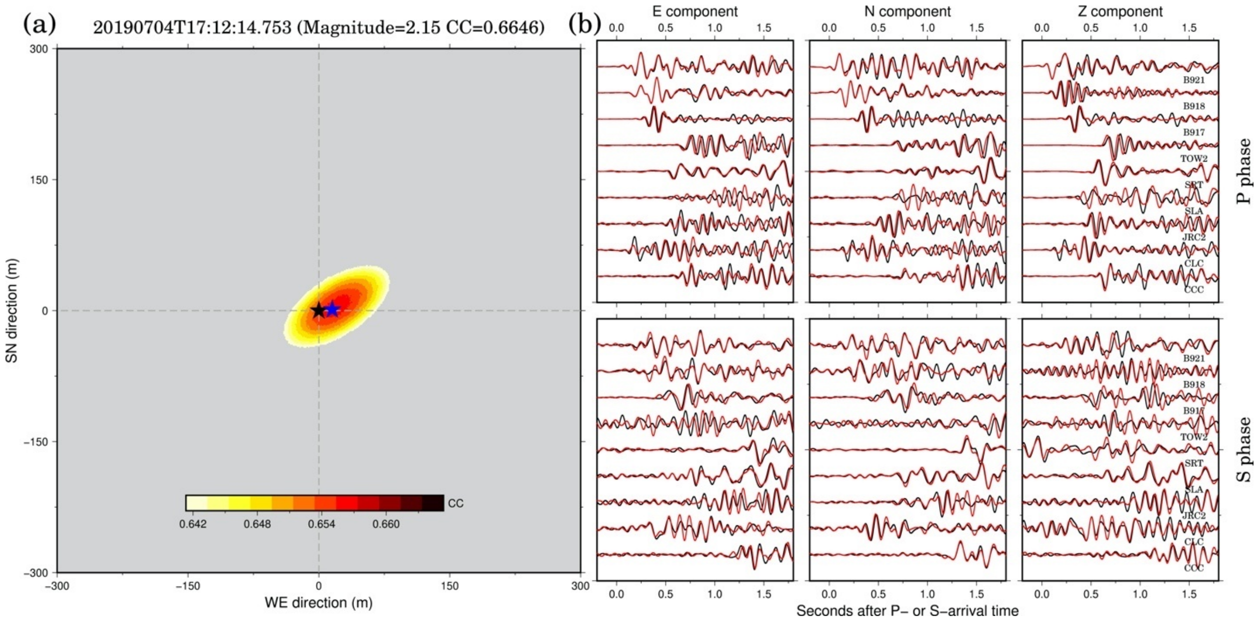

Figures S21. Smilar to Figure S5, but for EQ 18.

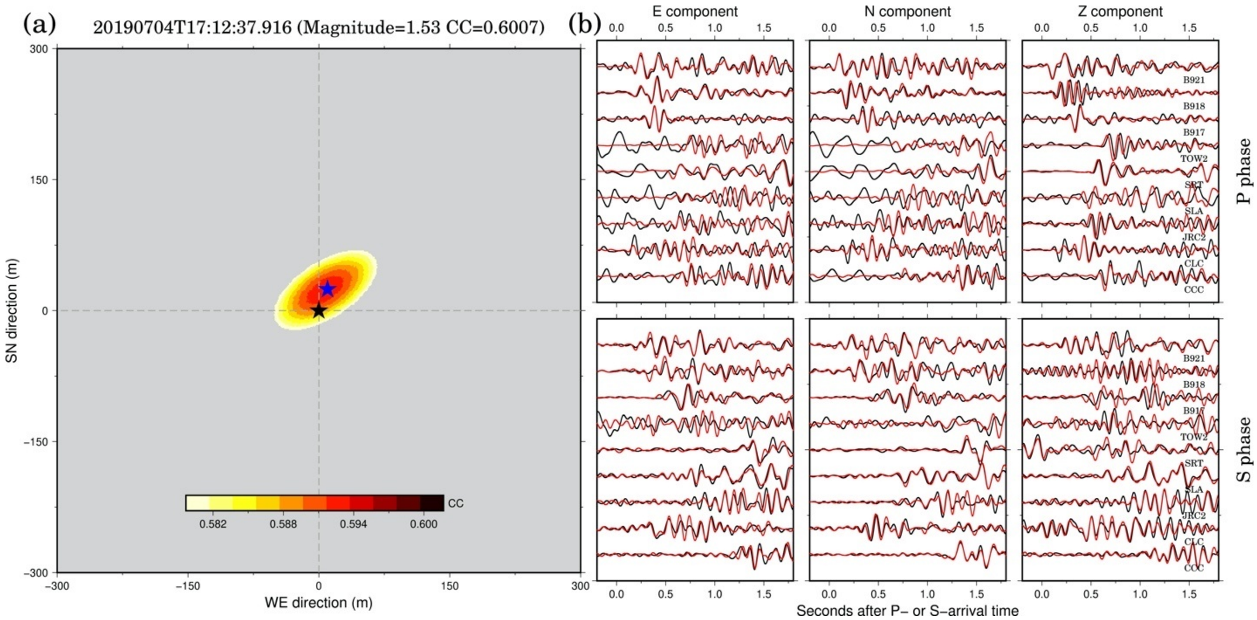

Figures S22. Smilar to Figure S5, but for EQ 19.

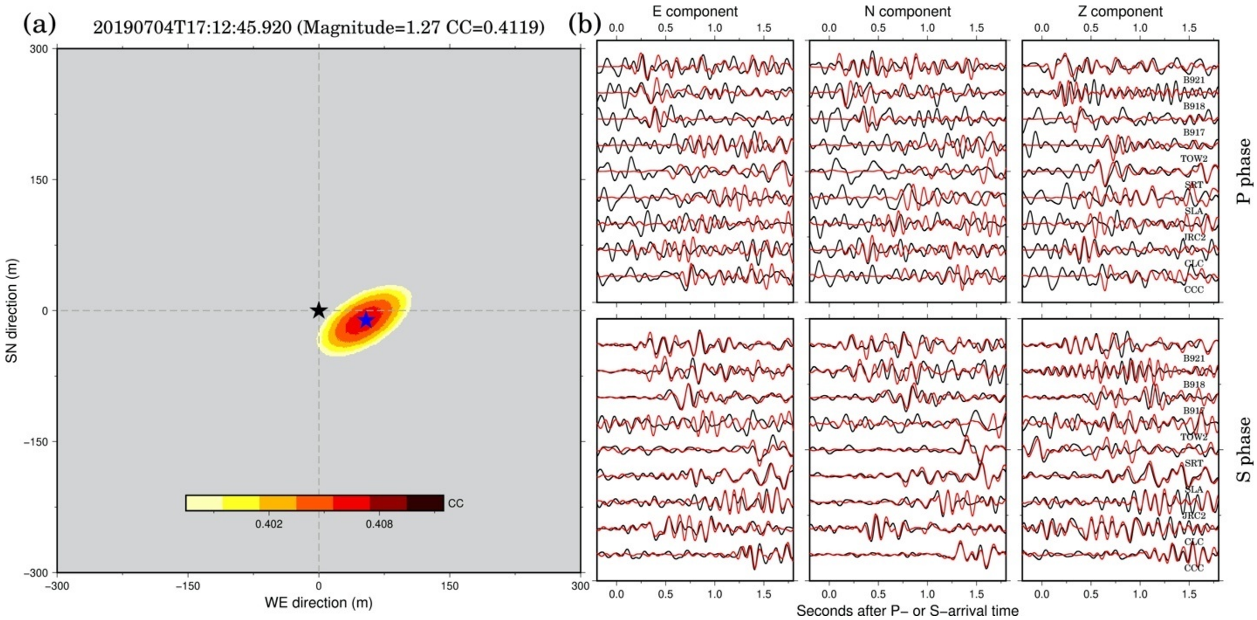

Figures S23. Smilar to Figure S5, but for EQ 20.

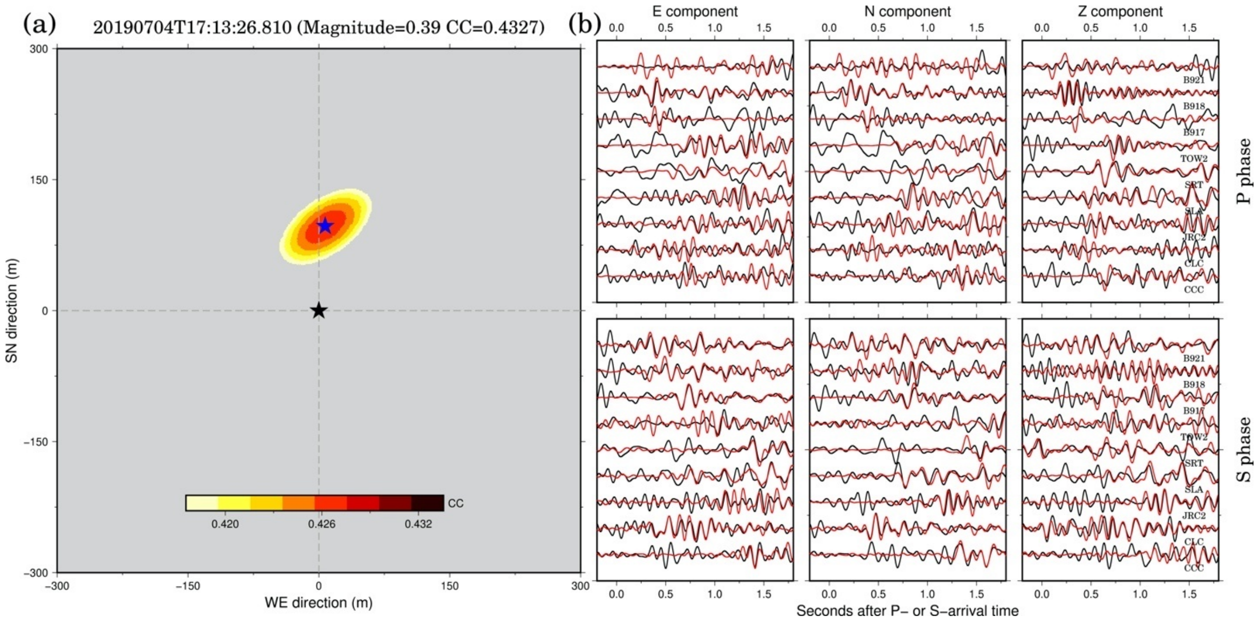

Figures S24. Smilar to Figure S5, but for EQ 21.

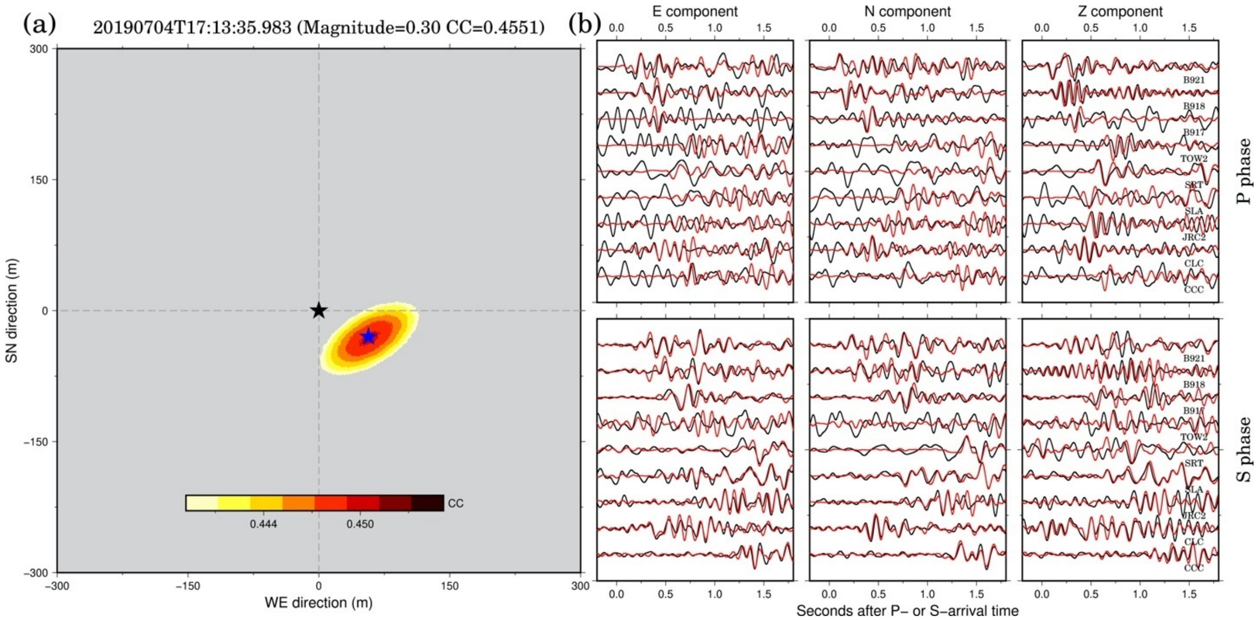

Figures S25. Smilar to Figure S5, but for EQ 22.

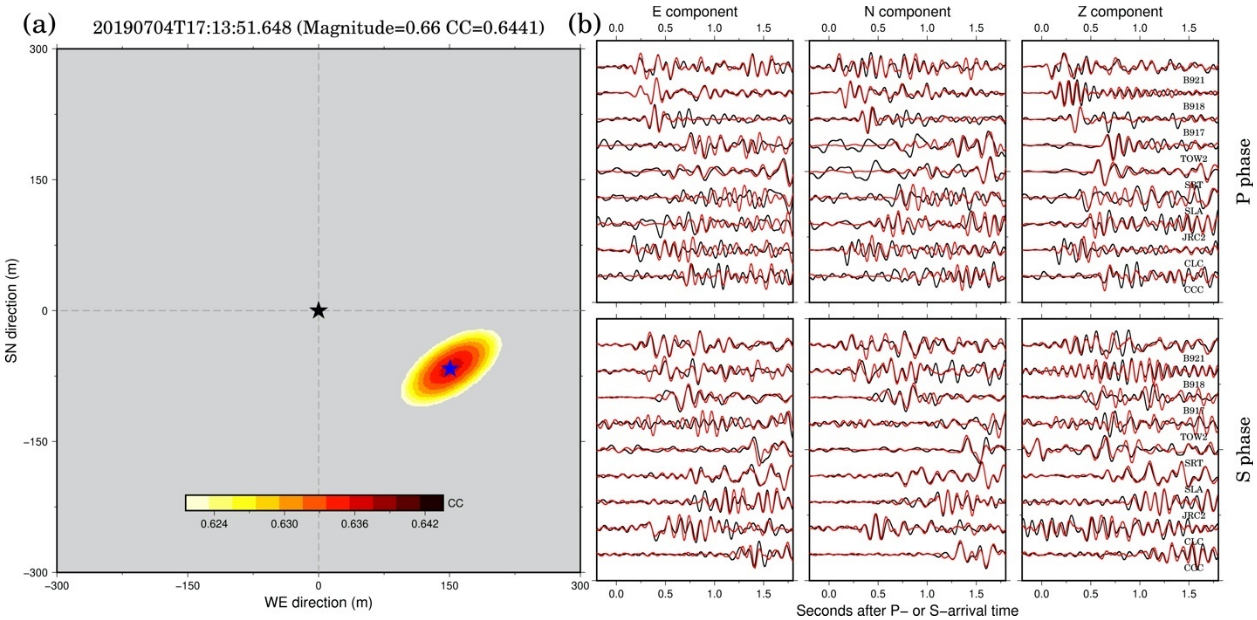

Figures S26. Smilar to Figure S5, but for EQ 23.

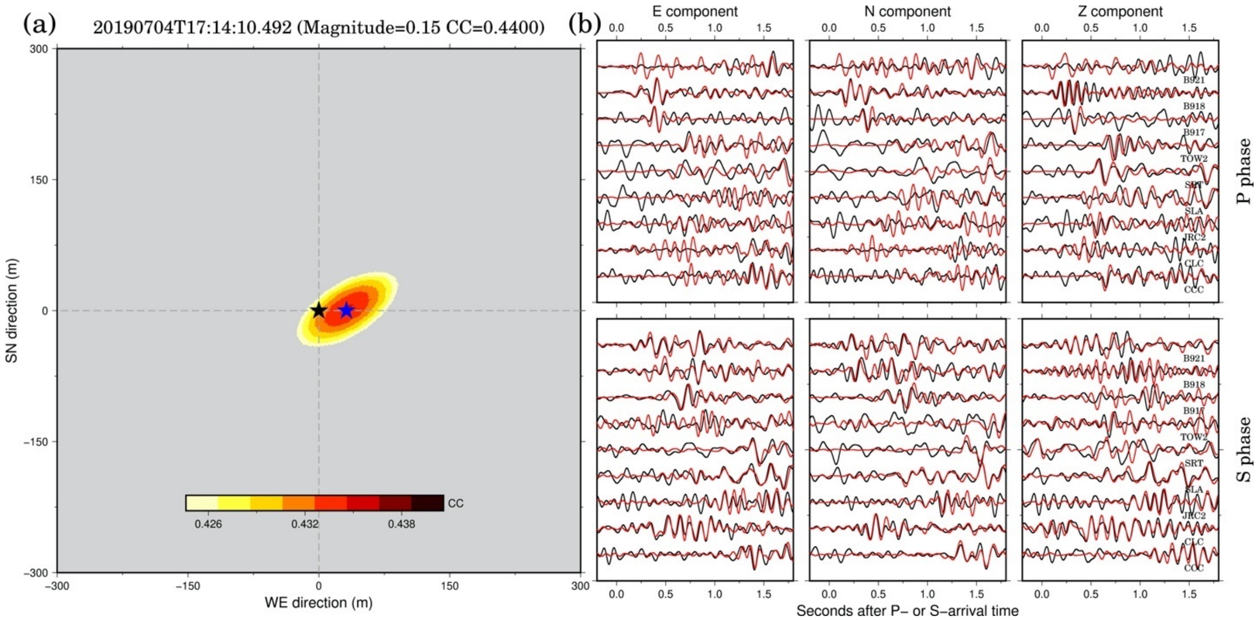

Figures S27. Smilar to Figure S5, but for EQ 24.

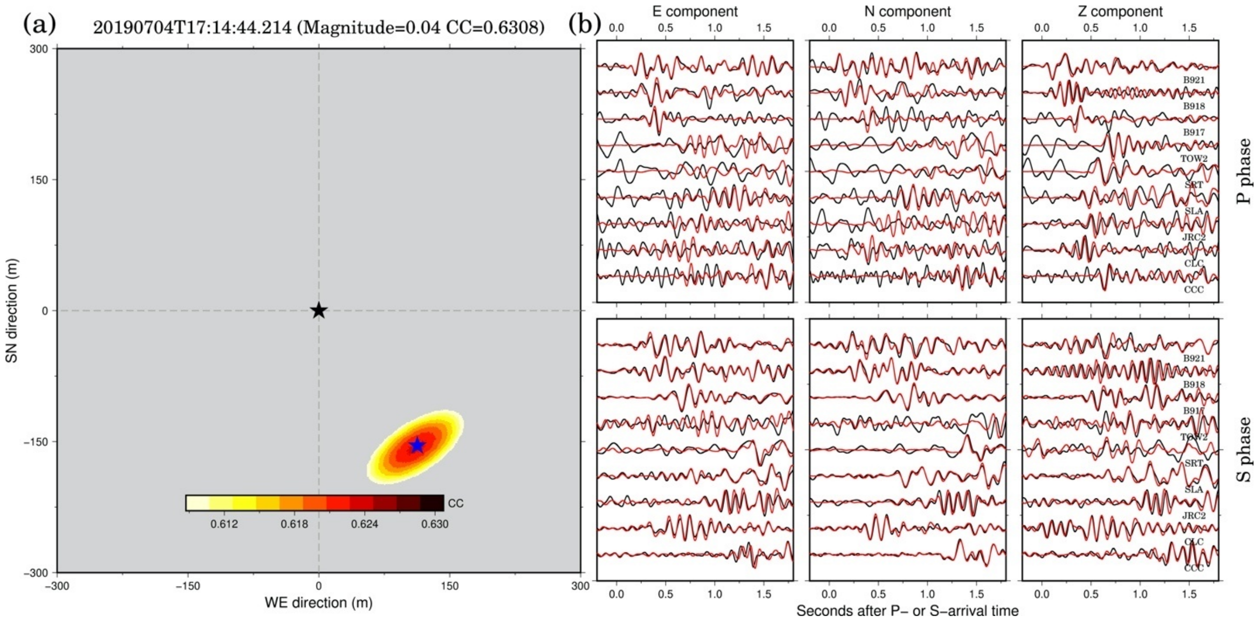

Figures S28. Smilar to Figure S5, but for EQ 25.

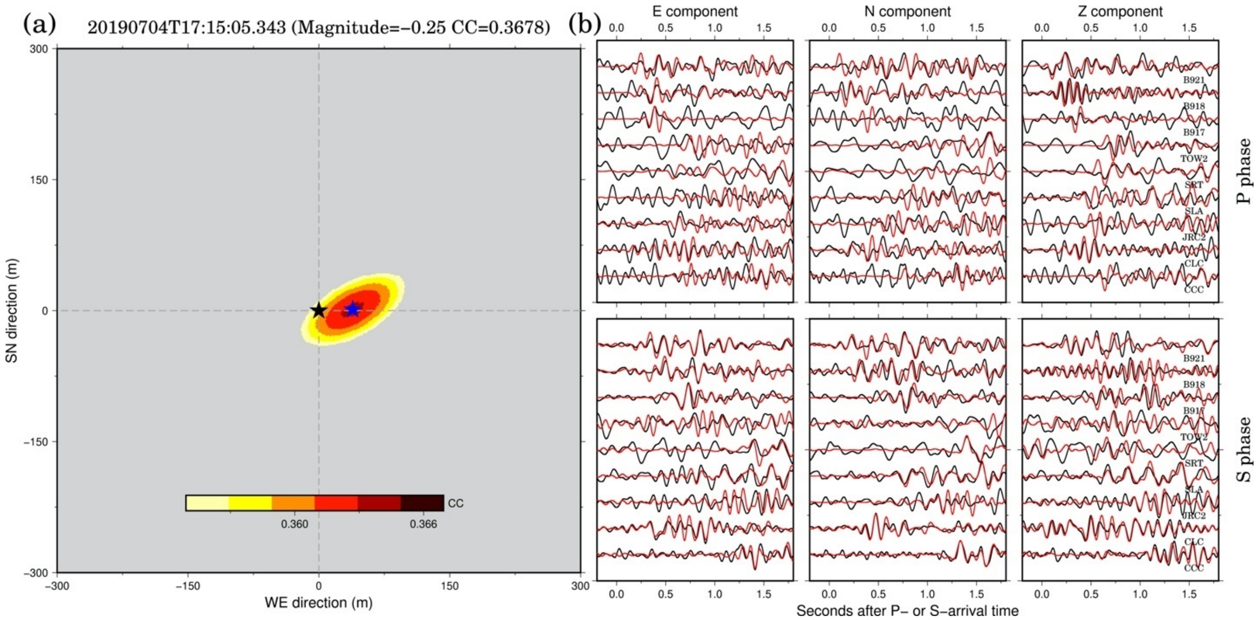

Figures S29. Smilar to Figure S5, but for EQ 26.

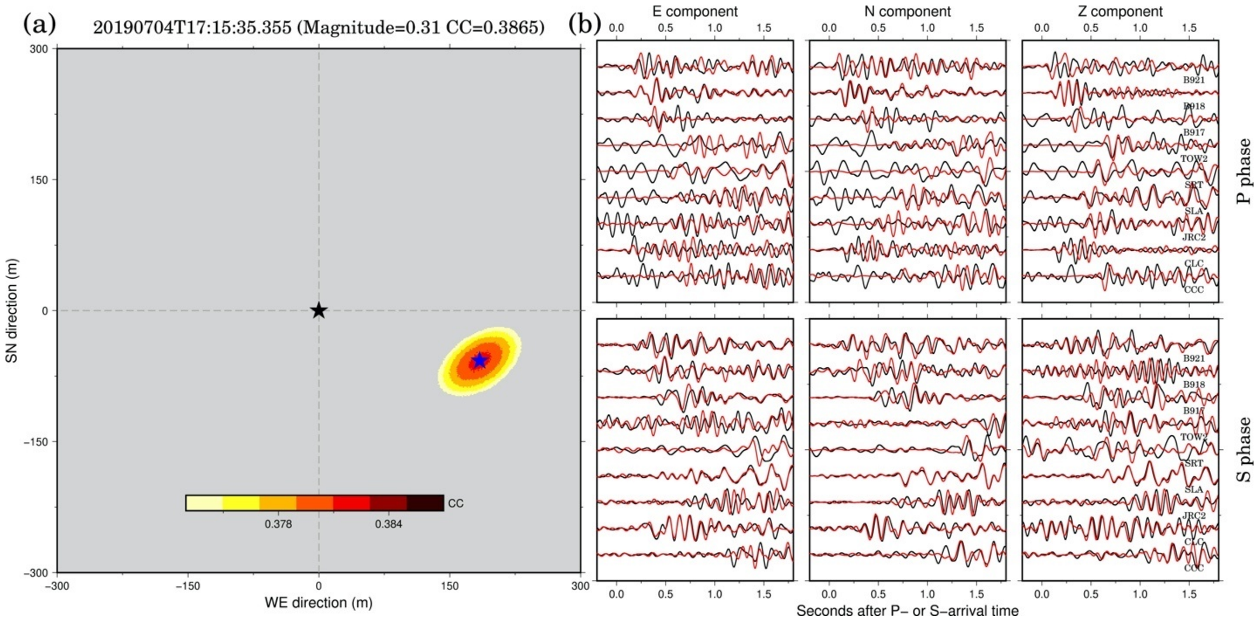

Figures S30. Smilar to Figure S5, but for EQ 27.

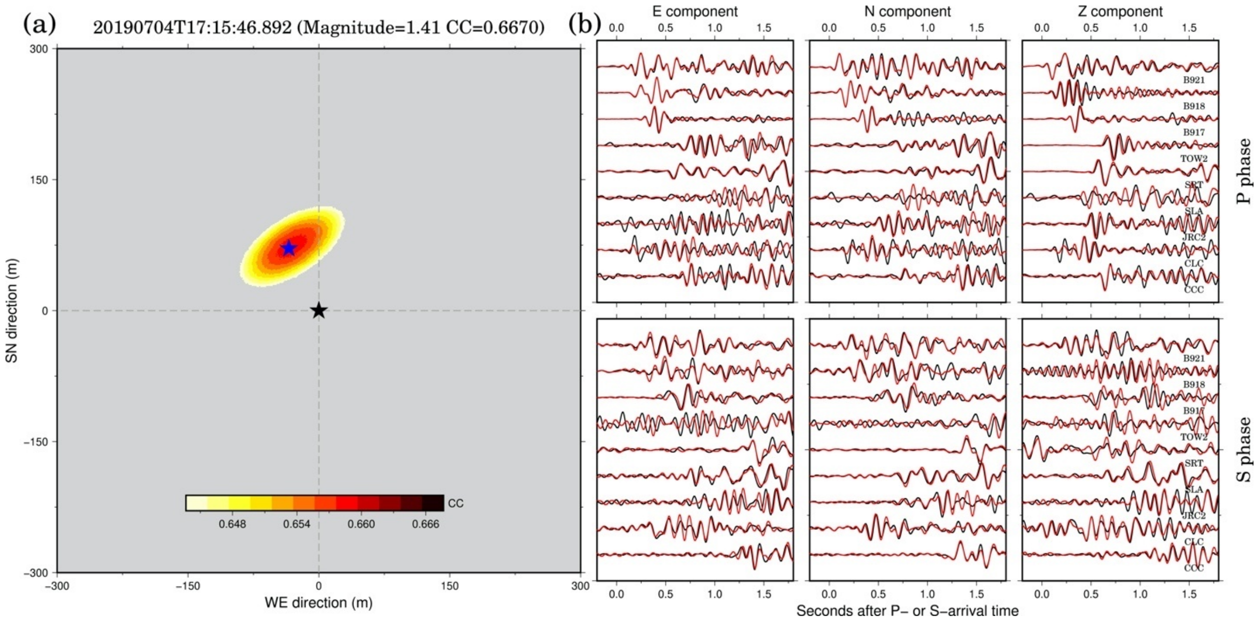

Figures S31. Smilar to Figure S5, but for EQ 28.

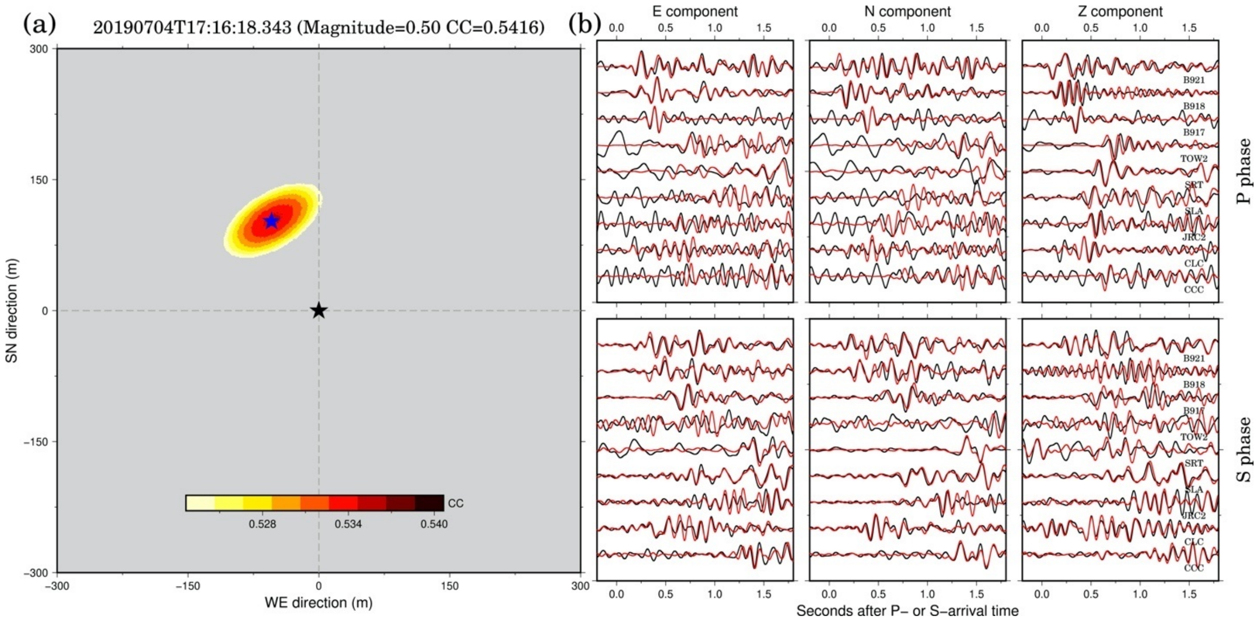

Figures S32. Smilar to Figure S5, but for EQ 29.

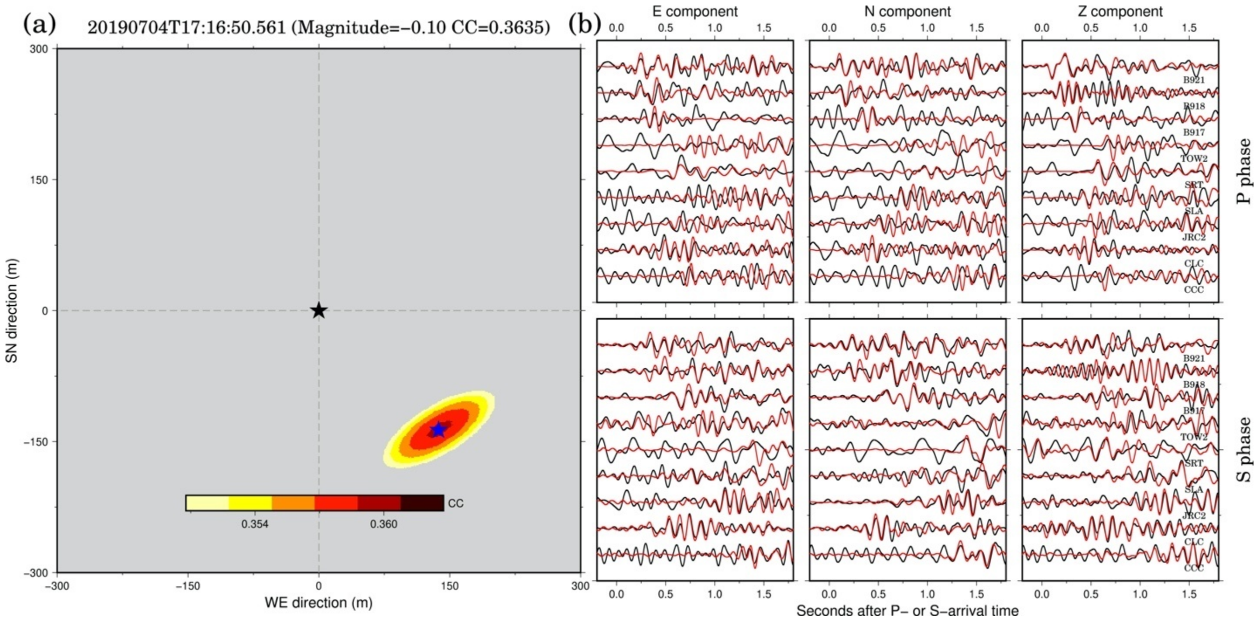

Figures S33. Smilar to Figure S5, but for EQ 30.

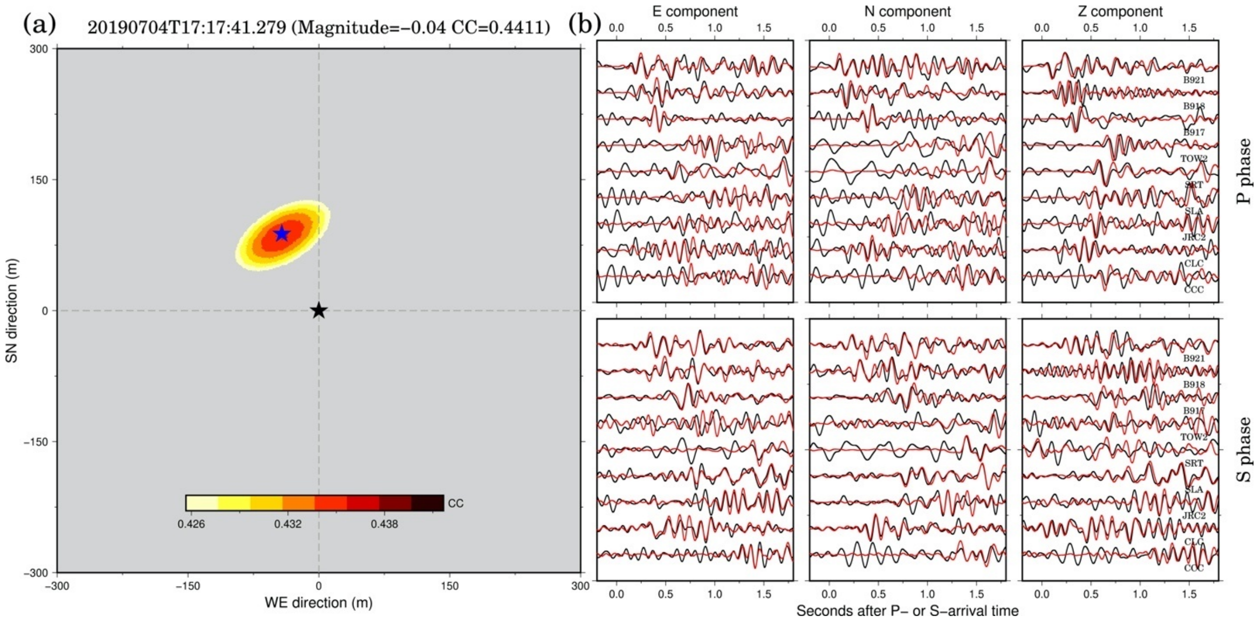

Figures S34. Smilar to Figure S5, but for EQ 31.

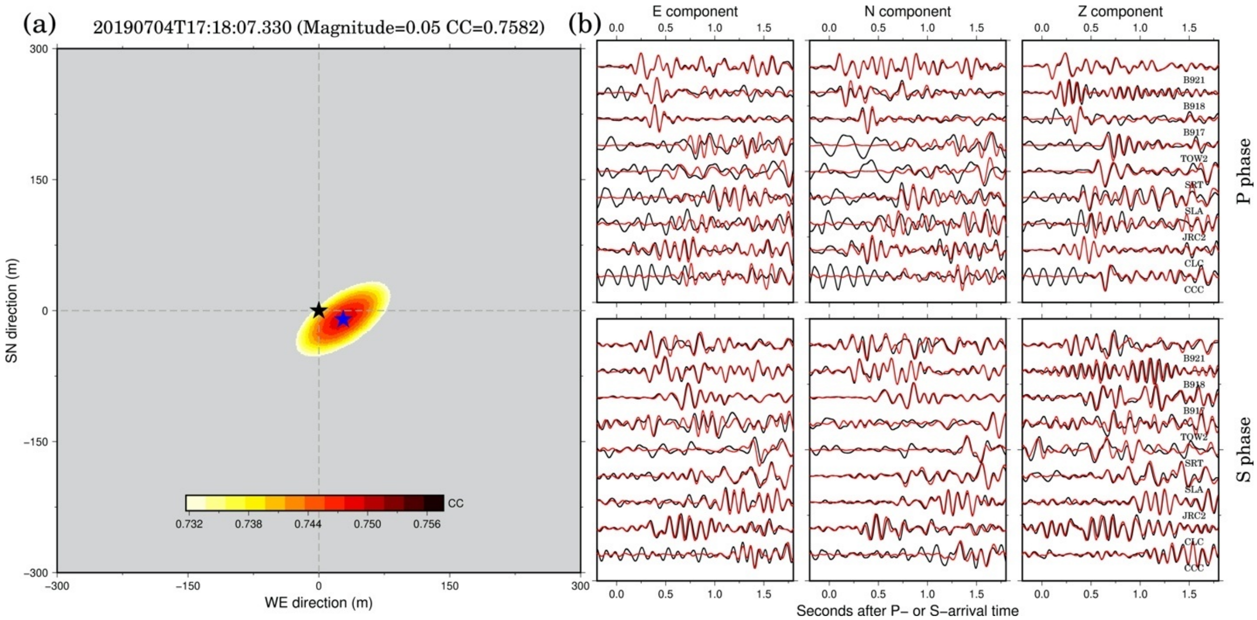

Figures S35. Smilar to Figure S5, but for EQ 32.

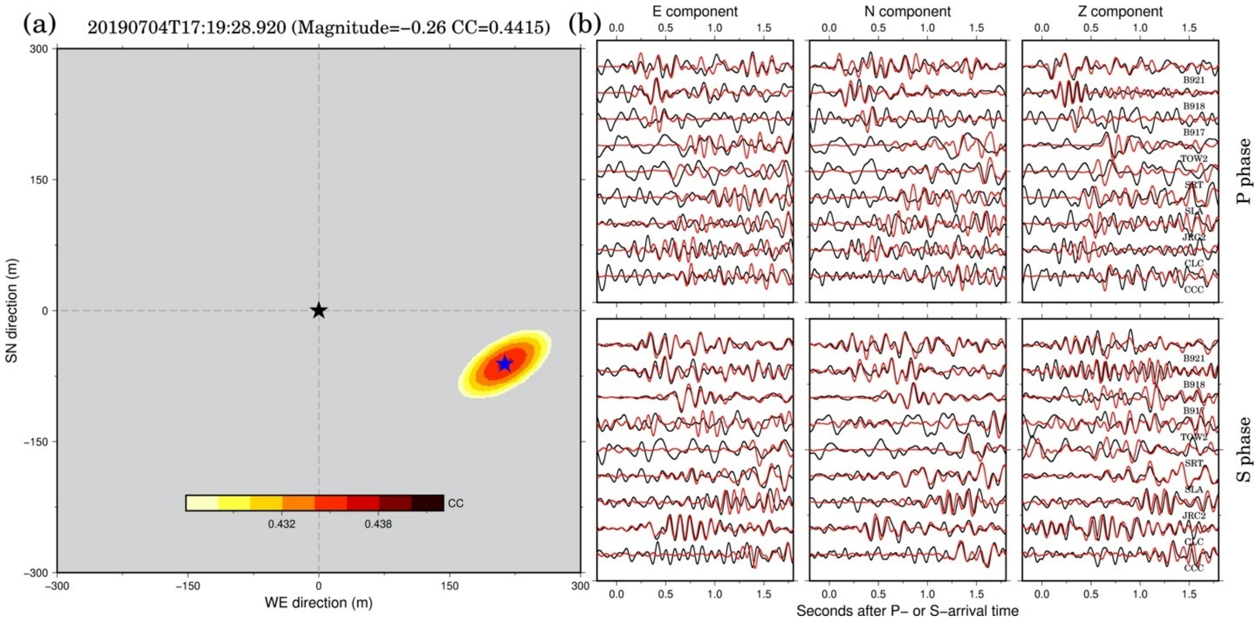

Figures S36. Smilar to Figure S5, but for EQ 33.

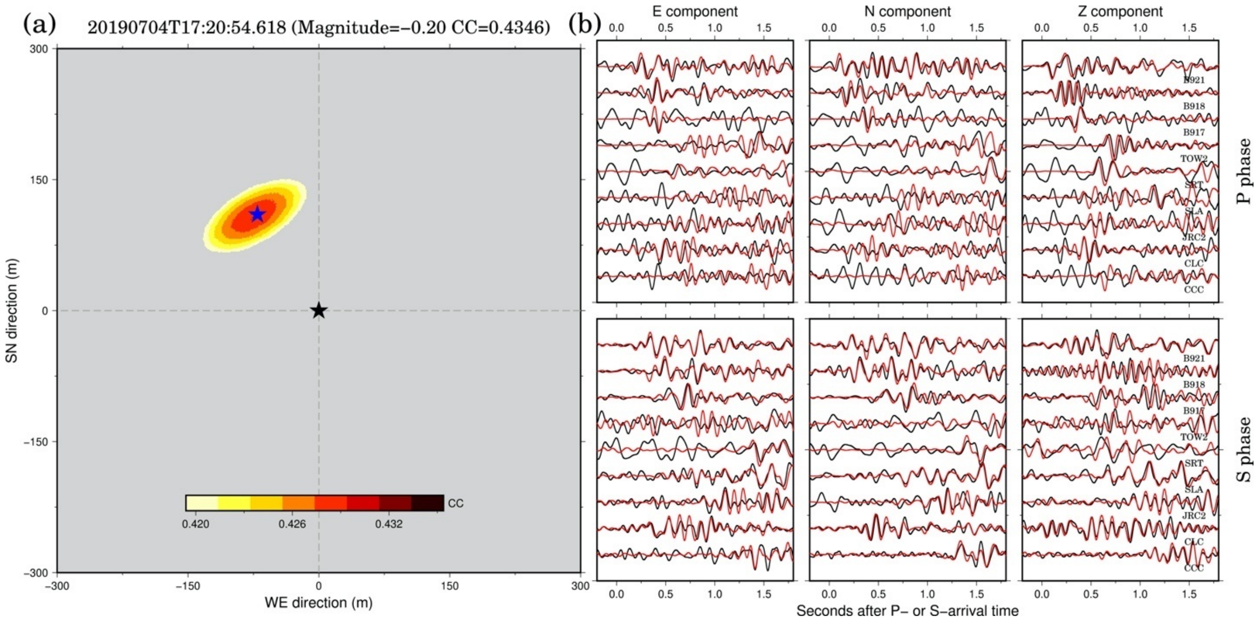

Figures S37. Smilar to Figure S5, but for EQ 34.

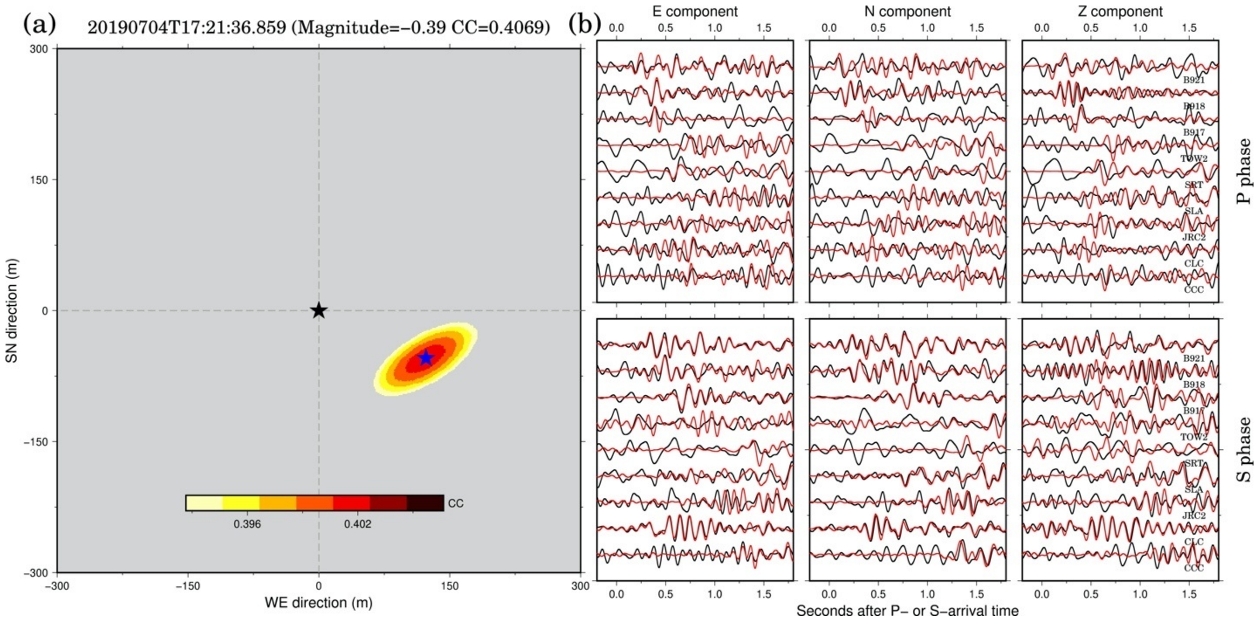

Figures S38. Smilar to Figure S5, but for EQ 35.

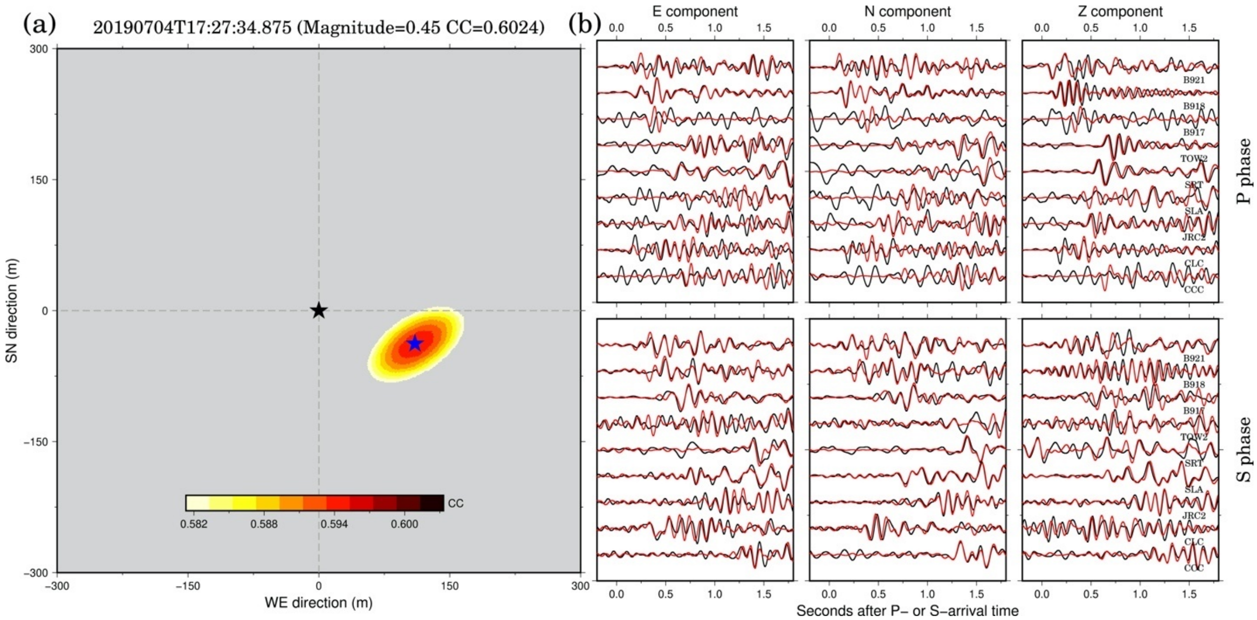

Figures S39. Smilar to Figure S5, but for EQ 36.

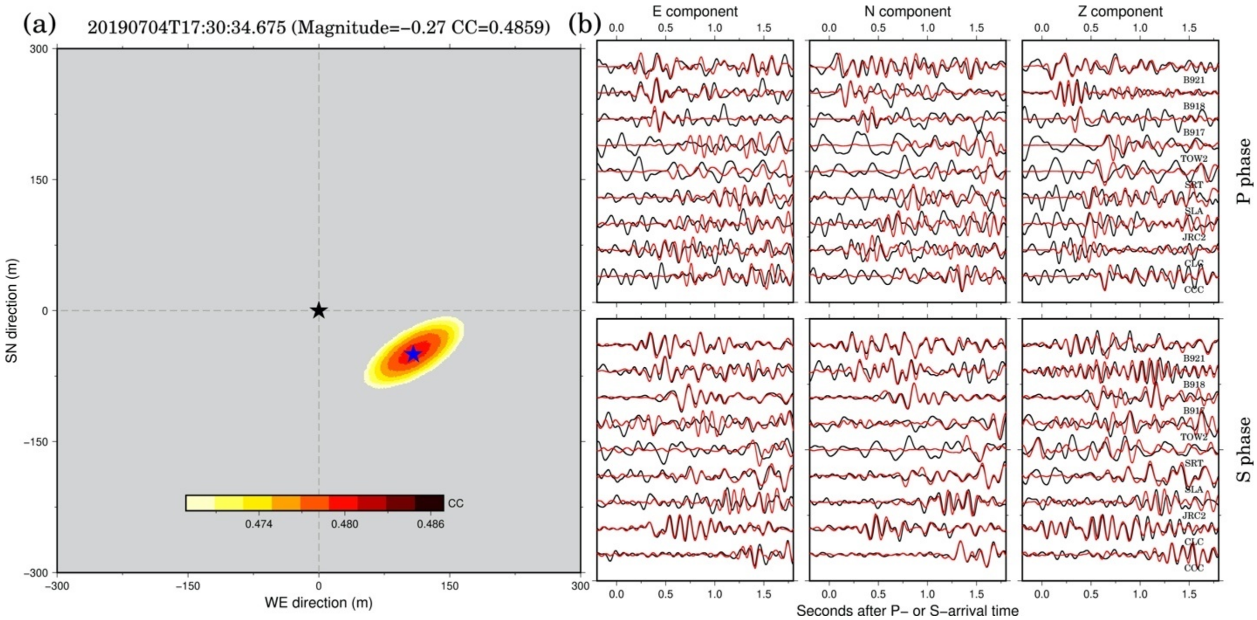

Figures S40. Smilar to Figure S5, but for EQ 37.

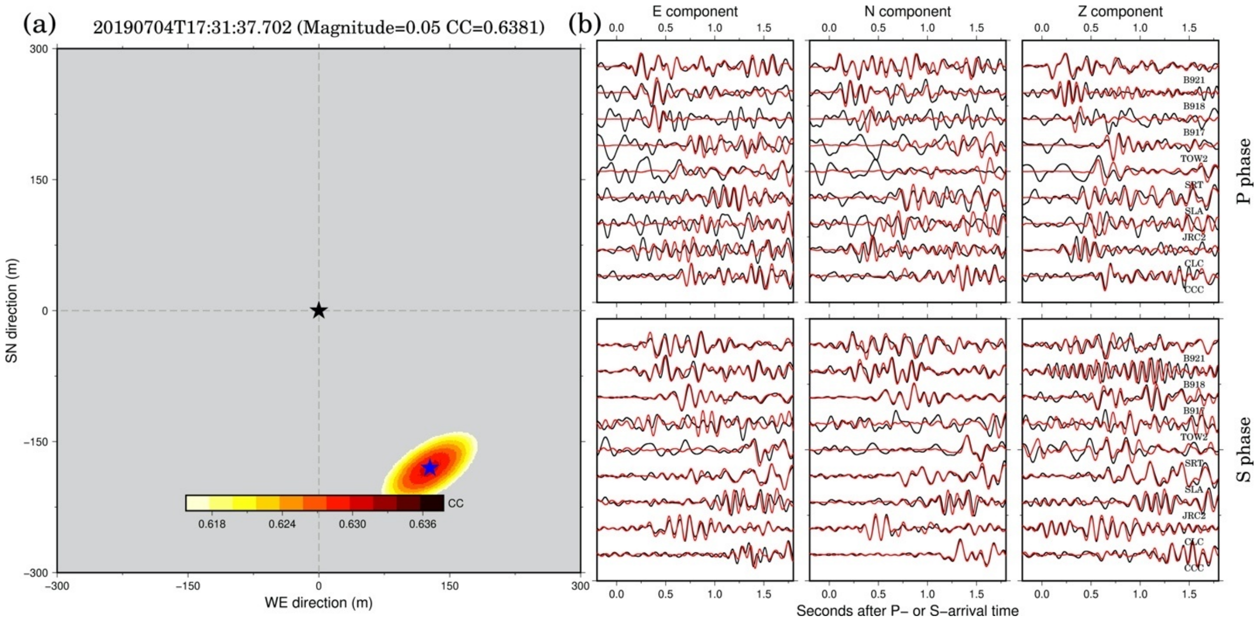

Figures S41. Smilar to Figure S5, but for EQ 38.

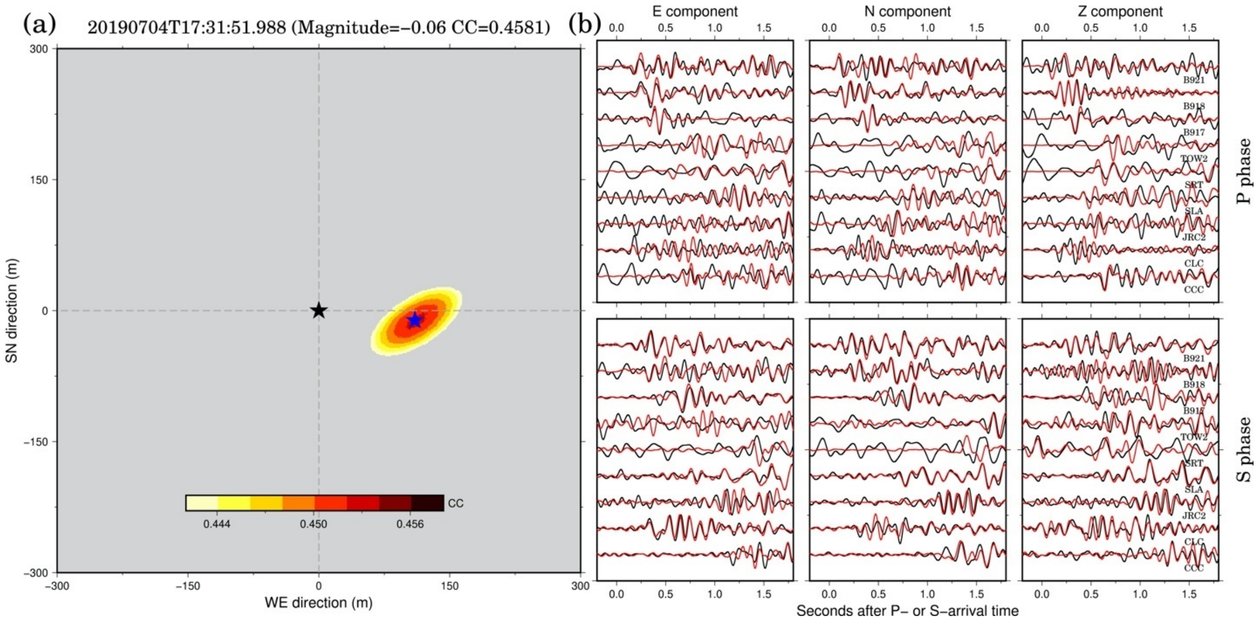

Figures S42. Smilar to Figure S5, but for EQ 39.

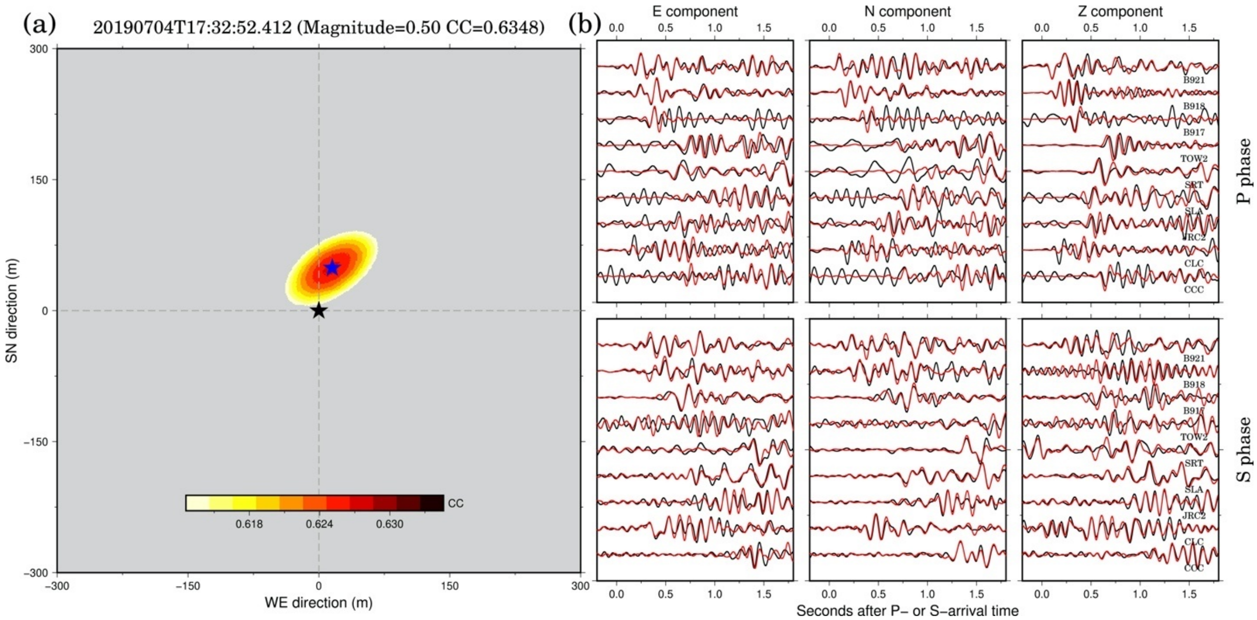

Figures S43. Smilar to Figure S5, but for EQ 40.

Table S1. The M&L foreshock catalog.

Movie S1. 3D movie showing detailed spatiotemporal distribution of these foreshocks listed in the M&L catalog (also see Figure 2).